INVESTIGATION OF A SELF-POWERED FONTAN CONCEPT USING A MULTISCALE COMPUTATIONAL FLUID-STRUCTURE INTERACTION MODEL

by

KYLE W. BEGGS
B.S. University of Central Florida, 2016

A thesis submitted in partial fulfilment of the requirements
for the degree of Master of Science in Mechanical Engineering
in the Department of Mechanical and Aerospace Engineering
in the College of Engineering and Computer Science
at the University of Central Florida
Orlando, Florida

Fall Term
2018

ABSTRACT

Congenital Heart Disease (CHD) occurs in about 1% (40,000) of newborn babies each year in the United States alone. About 10.9% (960) of whom suffer from Hypoplastic Left Heart Syndrome (HLHS) - a subset of CHD where children are born with a single-ventricle (SV). A series of three surgeries are carried out to correct HLHS culminating in the Fontan procedure where venous flow returns passively to the lungs. The current configuration for the Fontan results in elevated Central Venous Pressure (CVP), inadequate ventricular preload, and elevated Pulmonary Vascular Resistance (PVR) leading to a barrage of disease. To alleviate these complications, a 'self-powered' Fontan is suggested where an Injection Jet Shunt (IJS) emanating from the aorta is anastomosed to each pulmonary artery. The IJS attempts to reduce the central venous pressure, increase preload, and aid in pulmonary arterial growth by entraining the flow with a high energy source provided by the aorta. Previous computational studies on this concept with rigid vessel walls show mild success, but not enough to be clinically relevant. It is hypothesized that vessel wall deformation may play an important role in enhancing the jet effect to provide a larger exit area for the flow to diffuse while also being more physiologically accurate. A multiscale 0D-3D tightly coupled Computational Fluid Dynamics (CFD) with Fluid-Structure Interaction (FSI) model is developed to investigate the efficacy of the proposed 'self-powered' Fontan modification. Several runs are made varying the PVR to investigate the sensitivity of IVC pressure on PVR. IVC pressure decreased by 2.41 mmHg while the rigid wall study decreased the IVC pressure by 2.88 mmHg. It is shown that IVC pressure is highly sensitive to changes in PVR and modifications to the Fontan procedure should target aiding pulmonary arterial growth as it is the main indicator of Fontan success.

To my Mom, Dad, and Brother. This one's for you.

ACKNOWLEDGMENTS

This work would have been impossible without the help of Dr. Marcus Ni whom helped me get up to speed when starting this project. Thanks to Dr. Ray Prather for sharing his technical expertise in computational modeling. I want to thank Giovanna Rodriguez for her gracious help constructing these difficult CAD models. Special thanks to Dr. William DeCampli for his clinical expertise and guidance in this tough problem. Last but not least, thanks to Dr. Alain Kassab for whom I would not be able to accomplish this without his inspiration to get involved in this research. Thanks to all!

TABLE OF CONTENTS

LIST OF FIGURES

LIST OF TABLES

CHAPTER 1: INTRODUCTION

Where conventional medical approaches may not be providing adequate treatment, engineers can offer new perspectives where mechanics play a dominant role. One such case is cardiovascular disease and the application of hemodynamics (the study of blood flow) which is a direct subset of the study of fluid mechanics - a pillar of engineering theory. The identification of irregular hemodynamics using engineering metrics is the new paradigm in cardiovascular medicine. Parameters such as Wall Shear Stress (WSS), pressure, volume flow rate, and oxygen saturation can aid physicians in decision making and significantly improve patient outcomes. In particular, we can make use of Computational Fluid Dynamics (CFD) models to simulate surgical procedures, identify risk factors for disease, design more efficient medical devices, and use as more cost-effective and less invasive diagnostic tools [32, 35, 22, 30, 21, 8, 38, 33, 5].

Congenital Heart Disease (CHD) occurs in about 1% (40,000) newborn babies each year in the United States alone [37, 17]. About 10.9% (960) of whom suffer from Hypoplastic Left Heart Syndrome (HLHS) - a subset of CHD where children are born with a single-ventricle (SV). Under a normal circulation, the Left Ventricle (LV) pumps oxygenated blood through the body and returns de-oxygenated blood to the heart where the Right Ventricle (RV) then pumps to the lungs for re-oxygenation of the blood. Patients with HLHS have an under-developed LV and aorta. The anatomical differences are shown in figure 1.1.

Even after the required surgical interventions to correct HLHS, the mortality rate is 12% at 1 year and approaches 17% by 10 years [6]. Medical morbidity, loss of quality of life, and health care monetary expense associated with CHD are formidable. Total hospital costs for HLHS patients is upwards of $221,000 where 23% of the total cost is due to re-admissions [19]. Additional hospital costs for re-admissions for individuals with CHDs were $1.4 billion US dollars in 2004 (adjust-

ing for inflation, this amounts to about $1.9 billion US dollars). For privately insured individuals, this breaks down to about $30,000 US dollars per patient with costs rising for severe cases. Perhaps even more debilitating than medical costs are the lifestyle changes, emotional stress, family uncertainty, and parents being unable to return to work full-time.

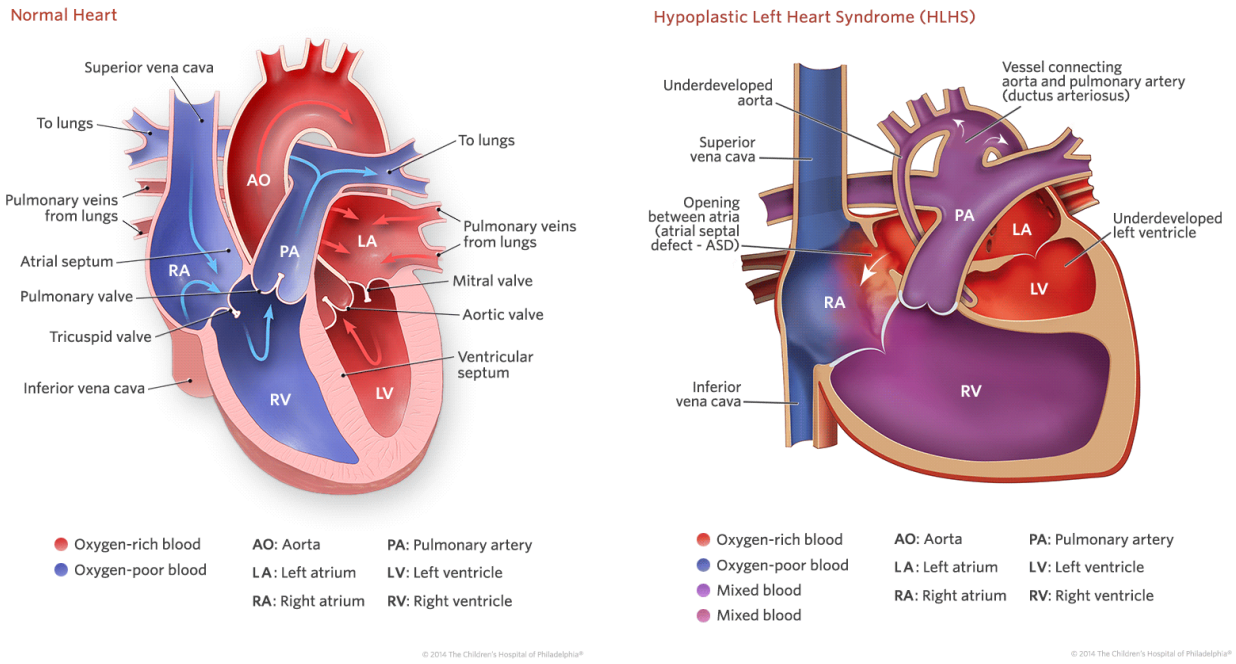

Figure 1.1: Normal and HLHS circulations

These children progress through a 3-stage surgical reconstruction culminating in the total cavo-pulmonary connection, or Fontan surgery [12]. The first procedure, termed the Norwood, reconstructs the aorta, patches the pulmonary artery, and introduces the Blalock-Taussig shunt. The second procedure, the Bi-directional Glenn, connects the Superior Vena-Cava (SVC) to the Right Pulmonary Artery (RPA) and severs the Blalock-Taussig shunt. The Norwood and Bi-directional Glenn surgeries are pictured in figure 1.2.

The third, and final, procedure is the Fontan. The Fontan establishes a serial circulation driven by the functioning SV where venous flow returns passively to the lungs bypassing the heart. Sev-

eral consequences include inadequate ventricular preload, elevated Pulmonary Vascular Resistance (PVR), and perhaps most debilitating - elevated Central Venous Pressure (CVP) (measured and referred to as the Inferior Vena-Cava (IVC) in this study). These hemodynamic conditions lead to an array of complications associated with the Fontan such as liver cirrhosis, protein-losing enteropathy, and plastic bronchitis [13, 14, 44, 29]. Freedom from death or complications are at only 31% at 20 years from implementation of the Fontan. Early-stage mortality has been overcome, yet late-stage survival rates remain dismal with a strong causative relationship between morbidity and Fontan failure/complications [23].

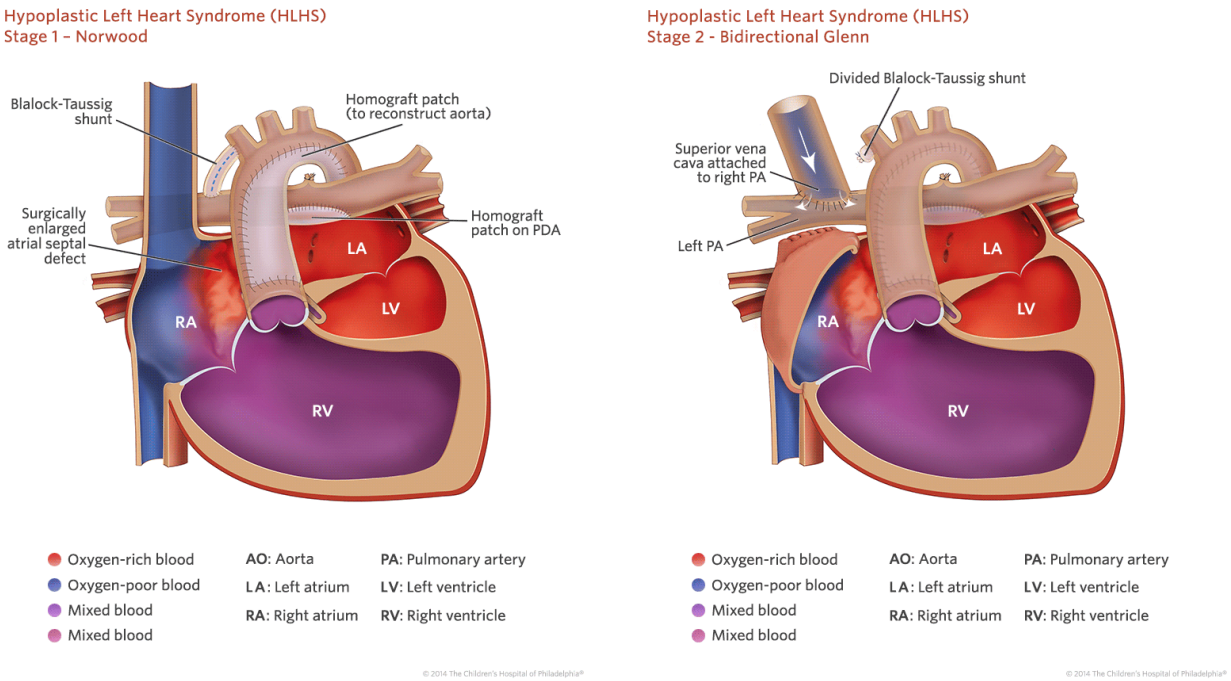

Figure 1.2: Norwood and Bidirectional Glenn procedures for correcting HLHS

These complications have plagued the Fontan procedure for years with minimal improvements. Even with the most expensive and intensive treatments, patients see improvements between 1-8%, where an improvement of 50-200% is optimal [13]. The statistics of Fontan complications can be seen in figure 1.4. With the maturation of computational power in the past 10 years came the possibilities to test unconventional ideas to aid the failing Fontan. Some of these include

geometrical modifications to the Total Cavopulmonary Connection (TCPC) diameter, location, shape, or the use of mechanical assist devices (powered pumps).

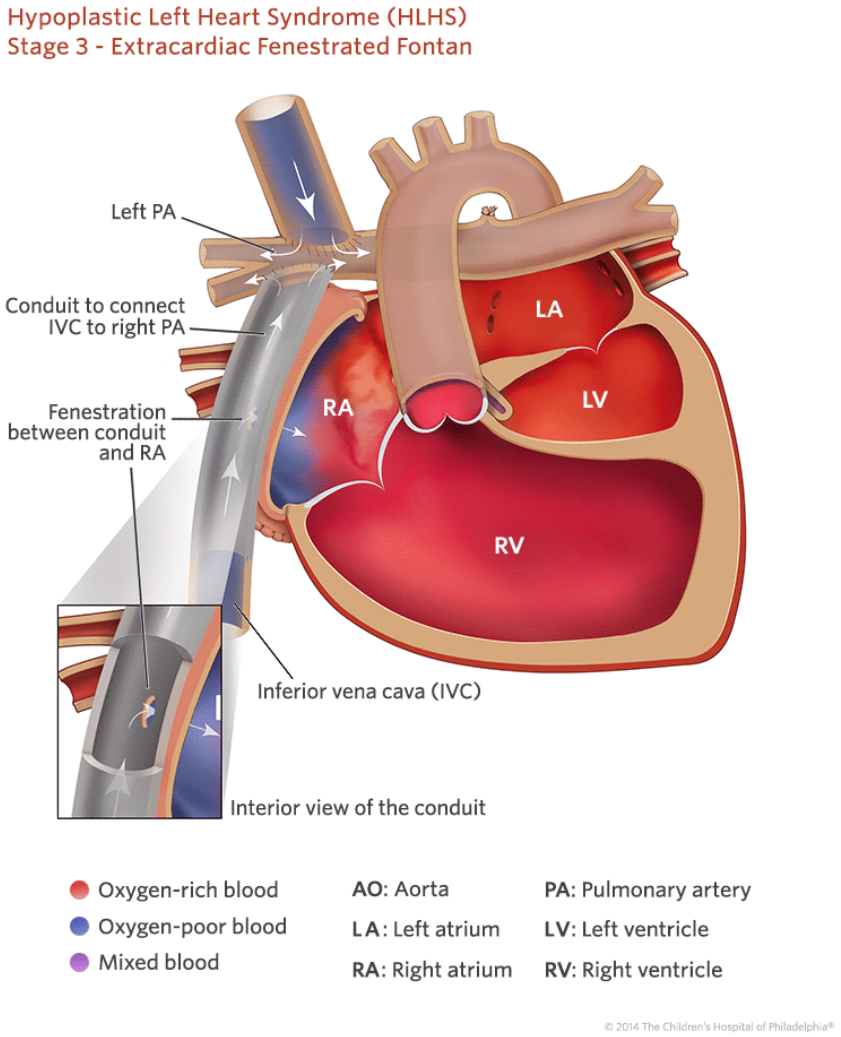

Figure 1.3: Fontan procedure

TCPC modifications such as a Y-shaped Inferior Cavopulmonary Connection (ICPC) or Glenn (Hemi-Fontan) shows minimal improvement over the conventional Fontan procedure. Assist devices have shown to theoretical decrease IVC pressure back to healthy values, but come at a cost. Current issues include increased risk for thrombosis, re-circulation, or suction at the inlet causing venous collapse. These issues lead to infection, embolisms, or stroke if a fenestration is created.

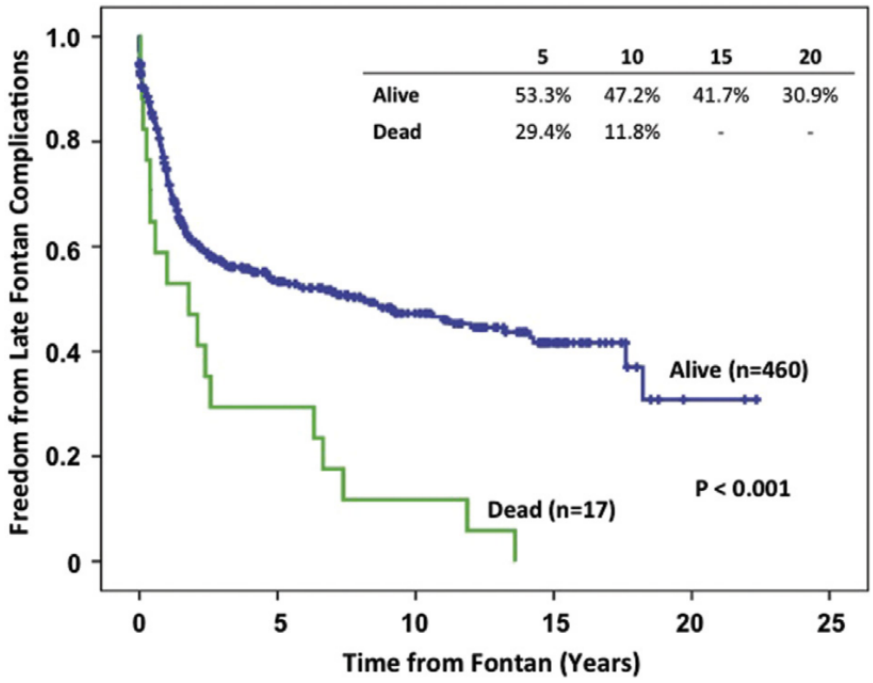

Figure 1.4: Freedom from complications in the Fontan. Taken from Kotani [23]

Our group has previously proposed a 'self-powered' Fontan modification where an Injection Jet Shunt (IJS) originates from the aorta, bifurcates once, and is anastomosed to each pulmonary artery to entrain the flow with a high-velocity jet [32]. It was shown to reduce IVC pressure, augment pulmonary flow to aid in pulmonary arterial growth (a major determinant of long-term Fontan success), and increase systemic O_2 delivery. Typically, injection jet pumps that take advantage of this phenomena open to a large reservoir at the outlet. This is the significant departure from the implementation of the IJS in Fontan patients as we know the cardiovascular system is closed to the atmosphere. This is a major limitation to the self-powered concept, but may be overcome.

It is proposed that this model may be underestimating the pressure drop due to the rigid wall assumption. If the arterial walls are made to be compliant, the outlet should expand giving room for the augmented flow from the IJS to exit without congestion. This would ultimately reduce the losses associated with this modification and further the reduction of pressure at the IVC.

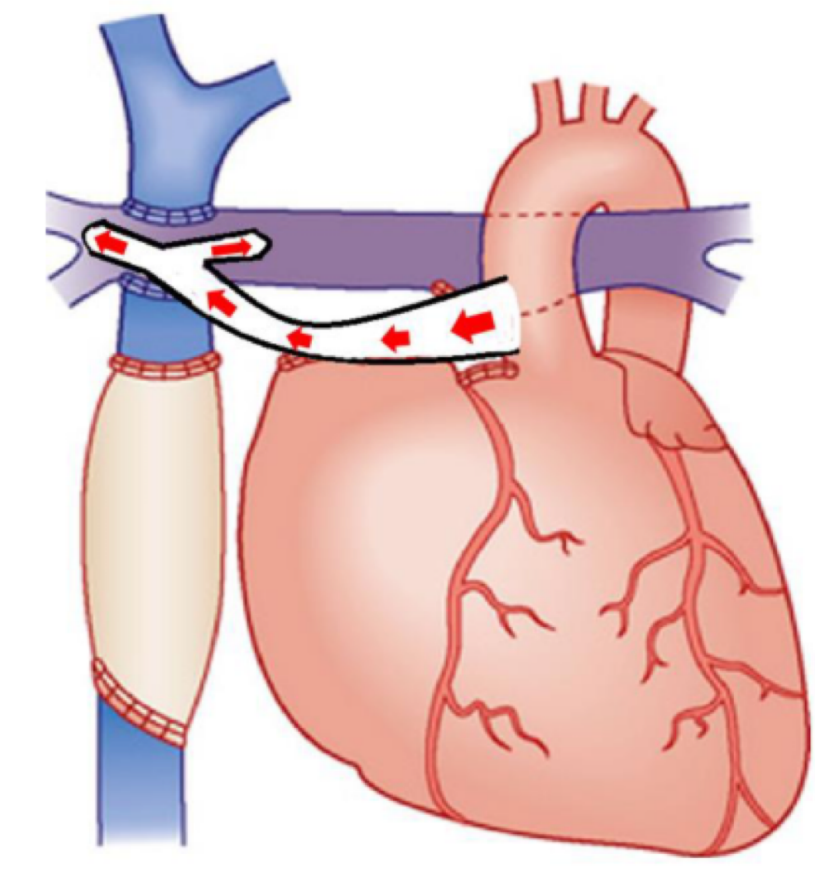

Figure 1.5: The Injection Jet Shunt (IJS) from the aorta to the pulmonary arteries

CHAPTER 2: LITERATURE REVIEW

2.1 The Fontan Circulation

The Fontan surgery was first introduced in 1971 by Francis Fontan, a French Cardiologist, to treat tricuspid atresia [12]. His proposition relies on post-capillary pressure to drive the venous return to the atrium, i.e. it is a passive system. This leads to an array of abnormal hemodynamics such as decreased Cardiac Output (CO) and elevated Central Venous Pressure (CVP). It is estimated that over a thousand Fontan surgeries are carried out each year in the US with 50,000-70,000 Fontan patients currently alive worldwide [39].

This population has seen a dramatic decrease in early-stage mortality with a 20 year survival rate of 92%. The average age for Fontan populations is expected to increase from 18 years old in 2014, to 23 years old in 2025, and 31 years old in 2045. In light of this, the focus of research on the Fontan procedure has shifted to late-stage complications. Gewillig, et al. [14, 13] has outlined the abnormal hemodynamic conditions (increased central venous pressure, decreased cardiac output) in the Fontan that lead to an array of late-stage complications such as liver cirrhosis - the most devastating. Yu, et al. [44] found there was low pulmonary vascular compliance leading to protein-losing enteropathy. Mitchell, et al. [29] found most Fontan patients had pulmonary vascular disease and that elevated Pulmonary Vascular Resistance (PVR) is a likely contributor to Fontan failure.

2.2 Multiscale Computational Modeling

The use of multiscale computer simulations to assess HLHS and specifically the Fontan has dominated the research landscape in recent years with no signs of slowing down. These computational models are accurate and typically robust. Simulations of HLHS anatomies require special treatment due to their unconventional physiology. Most simulations focus only on the systemic arterial or venous systems one at a time, but the Fontan requires modeling of both. This means a strict passing of information between the different scales (3D to 0D) in a tight-coupled manner, i.e. exchange information at every time step. This method was introduced by Quarteroni, et al. [36] where they led the 0D Lumped Parameter Model (LPM) over the 3D CFD in time.

Tightly-coupled schemes are subject to stability issues at the boundaries where the LPM fails to agree completely with the 3D CFD. Esmaily-Moghadam, et al. [11] alleviated these issues by inserting auxiliary elements such as inductors at the inlets of the 3D domain where mass flow conditions are prescribed and capacitors at the outlets where pressure conditions are prescribed. Esmaily-Moghadam, et al. [10] also looked into backflow stabilization techniques such as using Lagrange multipliers, constraining velocity to be normal to the boundary, and adding a stabilization term to the boundary nodes. They found using stabilization terms were the most effective and least computationally intensive. Ni [31] suggested extending the computational domain to stabilize the boundaries and paying only a small price more in computational cost.

2.2.1 Fluid-Structure Interaction (FSI)

Bazilevs, et al. [3] was the first to model Fluid-Structure Interaction (FSI) in for the Fontan anatomy. They built the vessel wall by solving the Laplace equation with boundary conditions such that it would produce a thickness of 10% of the local hydraulic diameter. He concluded that

FSI is significant when measuring Wall Shear Stress (WSS) and pressures. However, the cycle-averaged WSS and pressures were close to the rigid wall model. To the best of my knowledge, Long, et al. [25] has conducted the only other Fontan FSI study. They looked at using variable wall properties as a large section of the Fontan geometry is Gore-Tex conduit. They concluded that FSI has little effect on overall hemodynamics but is significant for estimations of Wall Shear Stress.

2.3 Fontan Modeling

There has been several attempts to correct the abnormal hemodynamics and associated diseases with late-stage Fontan patients. The first group set out to optimize the current Fontan configuration while other tried modifying it. Itatani, et al. [20] looked at optimizing the Fontan conduit (IVC) size and determined 16-18 mm is best, but that does little to improve Fontan performance. Alexi-Meskishvili, et al. [2] determined the age at which performing the Fontan operation is most suitable for a given conduit size. They determined that at 2-3 years old the extracardiac Fontan operation could be performed as the conduit size was suitable for adult hemodynamic conditions as well.

Hsia, et al. [18] looked at the diameter of the Total Cavopulmonary Connection (TCPC) as a optimization parameter and found that 20 mm is best. They also mention the importance of the local geometry of the Fontan as it is strongly tied to energy loss. Bove, et al. [4] and de Leval, et al. [7] also studied Fontan optimization coming up with similar conclusions. They also stressed the importance of local geometry in minimizing energy losses in the Fontan.

Marsden, et al. [27] studied the effects of exercise on Fontan performance and concluded that it is important to consider exercise when evaluating new Fontan designs. Marsden, et al. [26] then introduced a Y-shaped Fontan/IVC conduit which decreased pressure and encouraged even

pulmonary flow distribution left to right, but was not clinically significant.

2.4 Assist Devices

More recently, the majority of efforts have started to shift to using mechanical assists to aid the Fontan. Several groups have had success in this, but with some sever potential drawbacks. Delorme, et al. [9] performed a Large Eddy Simulation (LES) comparing the standard Fontan with a pump in the middle of the TCPC with much success in reducing the pressure. Lin [24] used a centrifugal pump and achieved clinically significant pressure drops. Shimizu, et al. [41] and Pekkan, et al. [34] also had success reducing IVC pressure. Shimizu used a partial assist while Pekkan assumed full assist with both studies using computational models to assess the pumps. Aside from concerns of thrombogenesis and pump failure, SVC pressure is often increased at the expense of reduced IVC pressure.

2.5 Pulmonary Vascular Resistance (PVR)

Pulmonary Vascular Resistance (PVR) is linked to late-stage Fontan failure. The reduction in Cardiac Output (CO) and pulsatility has been linked to pulmonary hypertension and congestion. Henaine, et al. [16] concluded that a lack of pulsatility in the pulmonary arteries dampens arterial growth and contributes to pulmonary vascular disease and elevated PVR. Goldstein, et al. [15] determined that PVR decreased with exercise, but there was not a strong link. Schmitt, et al. [40] conducted a clinical study trying to determine the relationship between flow and PVR. They administered dobutamine stress to simulate exercise conditions and increased volume flow. They found an inverse relationship where PVR decreased with increasing flow.

CHAPTER 3: METHODOLOGY

Analysis of the proposed modifications to the Fontan surgery will be carried out completely computationally. That is, using a multiscale (0D-3D) CFD model covering all aspects of the complex cardiovascular system. This approach allows quick, yet accurate solutions where the power is available to manipulate the geometry and hemodynamic conditions and re-run the simulations with little overhead. This chapter details every aspect of the model (e.g. geometry, boundary conditions generation, solver settings).

3.1 Anatomical Model

The first step in modeling the complex hemodynamics observed in the Fontan procedure is developing a physiologically-accurate anatomical model. Typically, geometric parameters are taken from Magnetic Resonance Imaging (MRI) data. Imaging techniques include standard MRI, Phase Contrast MRI (PCMRI), and Computed Tomography (CT) which is sometimes referred to as Computerized Axial Tomography (CAT). Any of these images work for the purpose of 3D geometrical reconstruction, as this process relies only on the images themselves to segment out the geometry of interest.

This is a highly manual process which requires significant understanding of the imaging technique used and anatomy in the region of interest. The recent adoption of machine learning in industry has infected the healthcare sector and is being used to automatically segment these geometries to be used in computer simulations. There is reason to believe this process will be fully-automated in the near future, but remains highly-manual until the technology matures.

Considering the objective of this study, we can avoid this tedious process and construct a synthetic

model using average values from similar Fontan reports [28, 7, 20]. The Injection Jet Shunt (IJS) bifurcates and is virtually sutured to each pulmonary artery. Each IJS is 2.75mm in diameter as computed from the recommended area ratio (A_{IJS}/A_{pulm} where A_{IJS} is the area of the IJS and A_{pulm} is the area of the pulmonary artery) given a pulmonary artery of 12mm diameter [32]. Although a synthetic model is used in this study, analysis of patient-specific models is forthcoming. The CAD models are shwon in figure 3.1.

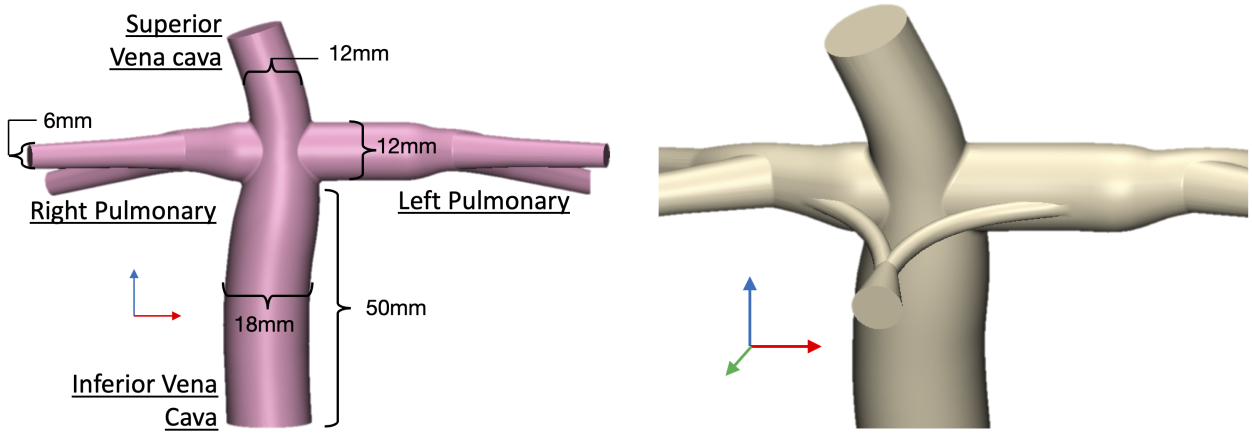

Figure 3.1: Synthetic geometries constructed. Left is the nominal case and right has the IJS

3.1.1 Creating the Vessel Wall

After creation of the synthetic model using Dassault Systemes SolidWorks 3D CAD software, the geometry was imported into Materialise 3-matic (3D CAD program specializing in medical applications) for creation of the vessel wall. Modeling the wall correctly is imperative to performing an accurate Fluid-Structure Interaction (FSI) simulation. The thickness was taken to be 10% of the *local* hydraulic diameter as per common practice. Only the pulmonary arterial walls were modeled and included in the simulation because the IVC is assumed to be rigid (see section 3.3.2 for a detailed explanation). The solid (vessel wall) domain is shown in figure 3.2.

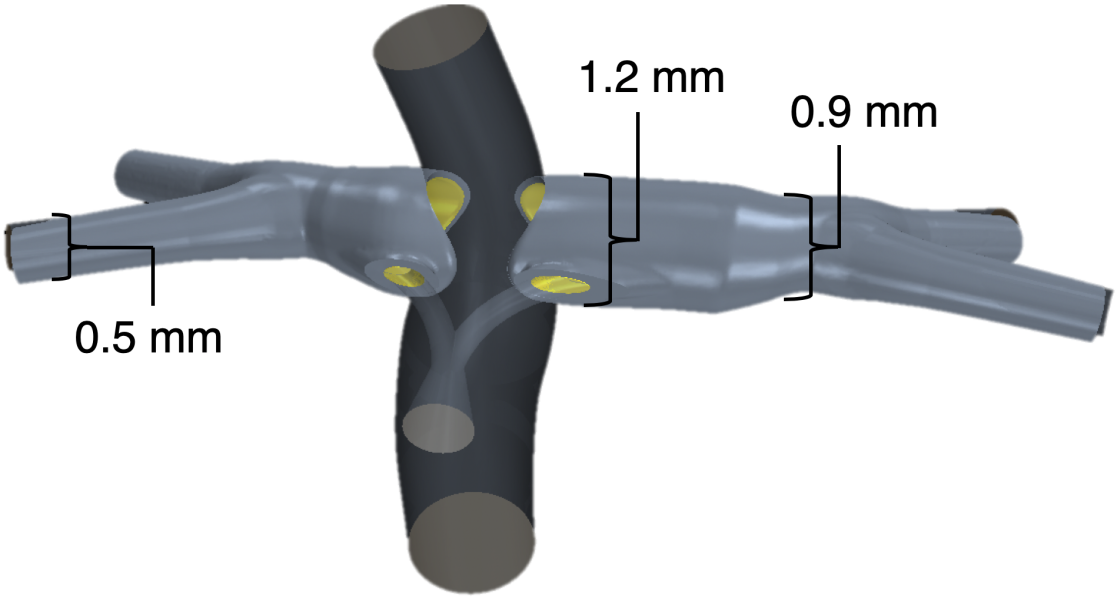

Figure 3.2: The portion of vessel walls included in the model

3.2 0D Hemodynamic Model

At the heart of every CFD calculation lie the boundary and initial conditions. The results are a direct outcome of boundary conditions prescribed and are especially critical in hemodynamic simulations. It is arguably the most important parameter of the model and thus study overall. The human vascular system is an expansive network of bifurcating arteries and converging veins that range in size from about 20mm in diameter (the aorta, artery that stems directly from the heart) to 5 μm (capillaries, where oxygen is delivered to its final destination). The length of all the vessels in the body combined is estimated to be over 60,000 - 100,000 miles [1]! As the size of geometry to be used in CFD simulations grows, so does the computational 'cost' (CPU time). It would be almost impossible to simulate the entire system in a time-dependent 3D manner, which is required for this problem as well as most others performing surgical planning/optimization simulations.

Thankfully, several analogies can be drawn between blood flow and electrical circuits. The vasculature endures an impedance to the flow, which acts in the same manner as electrical impedance.

This can be represented by several components - namely a resistor, capacitor, inductor, and diode. The analogy begins with Ohm's Law for electrical circuits

$$\Delta V = IR \quad \rightarrow \quad \Delta p = QR \tag{3.1}$$

where the voltage difference (ΔV) is like the pressure drop over a distance in the vessel (Δp) and the current (I) is like the volume flow rate of blood through that same segment of vessel (Q). The circuit elements can be described in mathematical form as

$$\Delta p = QR \quad \rightarrow \quad R = \frac{8\mu l}{\pi r^4} \tag{3.2}$$

$$Q = C\frac{dp}{dt} \quad \rightarrow \quad C = \frac{3\pi l r^3}{2Eh} \tag{3.3}$$

$$\Delta p = L\frac{dQ}{dt} \quad \rightarrow \quad L = \frac{9\rho l}{4\pi r^2} \tag{3.4}$$

where μ is the blood viscosity, l is the length of the vessel, r is the radius of the cross-section, E is the Young's Modulus, and h is the vessel wall thickness. The qualitative version of this analogy is shown in figure 3.3.

(a) Compliance (Capacitance) (b) Fluid Resistance (Resistance) (c) Inertia (Inductance)

Figure 3.3: The physical meaning of each circuit element

The analogies for the circuit elements are as follows: resistors model the time-averaged vessel resistance (equation 3.2), capacitors model the vessel wall deformation (equation 3.3), inductors model the blood inertia (equation 3.4), and diodes model valves. These elements can be lumped

together to re-create the physics of flow through an arterial or venous segment as seen in figure 3.4.

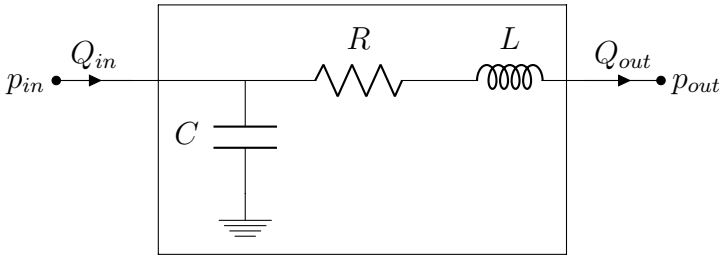

Figure 3.4: Circuit analog of an arterial/venous segment

It is simple to extend this for the complete vasculature - simply repeat the segments and include diodes and an 'electrical' heart by way of a forcing function. The forcing function is a time-varying capacitor where the capacitance is taken to be the inverse of the elastance ($C(t) = E(t)^{-1}$). The elastance can be interpreted physically as the contraction of the myocardium (heart wall) and takes mathematical form as the 'double-hill' function

$$E(t) = E_{max}\left[\frac{\left(\frac{t}{\alpha_1 T}\right)^{n_1}}{\left(1+\frac{t}{\alpha_1 T}\right)^{n_1}\left(1+\frac{t}{\alpha_2 T}\right)^{n_2}}\right] + E_{min} \tag{3.5}$$

where E_{max}, E_{min}, α_1, α_2, n1, n2 are all parameters that control the shape and magnitude of the elastance curve for the heart (specifically the RV in the case for HLHS patients with a single ventricle) [43].

Putting this all together we obtain a full 0D model fo the vasculature of interest which is typically referred to in the literature as a Lumped Parameter Model (LPM). For the self-powered Fontan concept we are testing, the LPM appears in the form shown in figure 3.5.

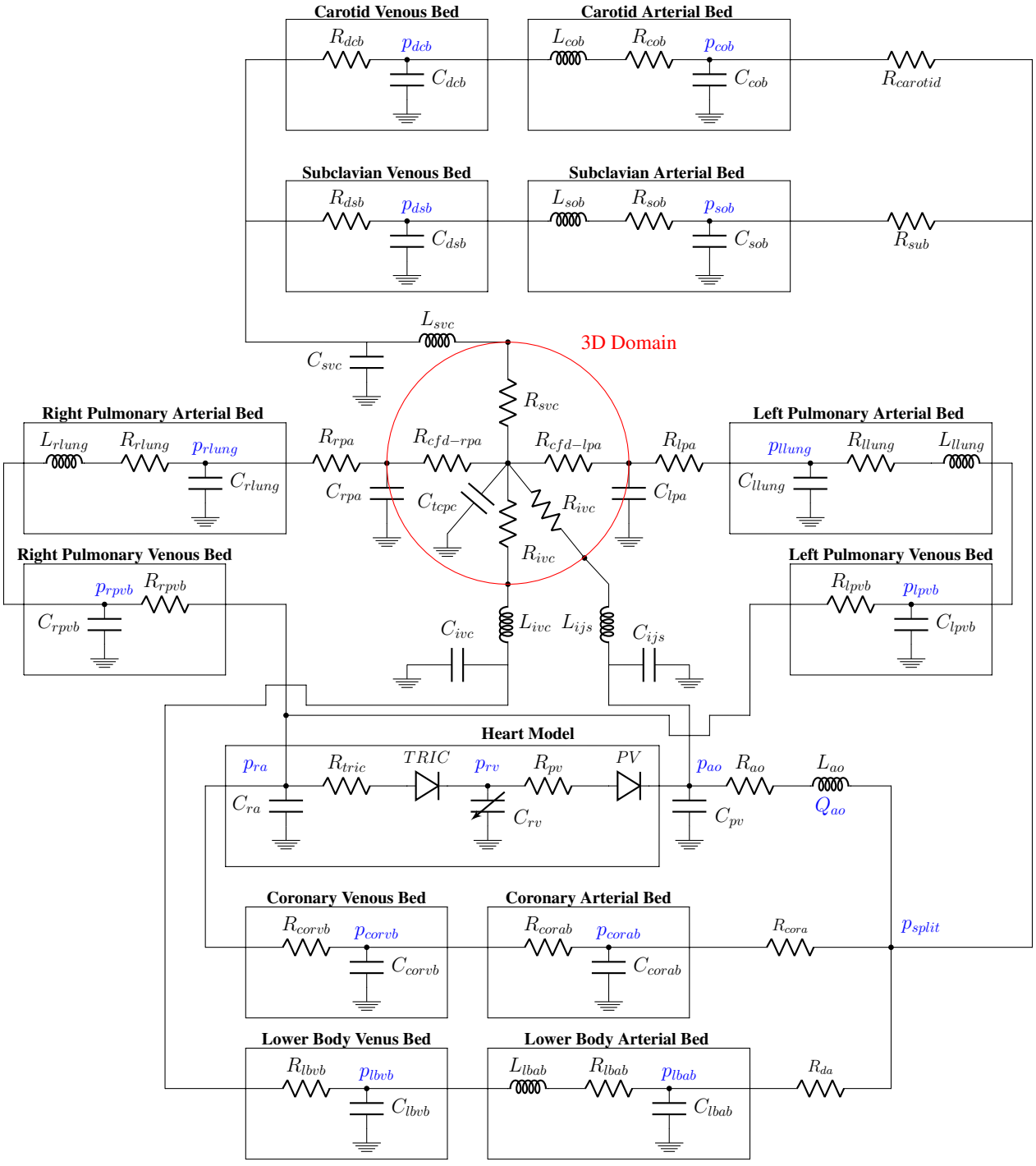

Figure 3.5: LPM diagram to initialize the solution

3.3 3D Hemodynamic Model

The 3D portion of the multiscale model is necessary in order to capture the complex 3D hemodynamics and momentum transfer of the IJS. This is done using a commercial CFD code, STAR-CCM+ ©. The anatomical model (described in 3.1) is exported from the CAD software as a surface mesh using the stereolithography (.stl) format and then imported into STAR-CCM+.

3.3.1 Fluid Domain: Computational Fluid Dynamics Model

The volume mesh is then created using polyhedral elements for both the fluid (blood) and solid (vessel wall) domains. Polyhedral cells were specifically chosen because the fluid solver is written using the finite-volume (FV) method and it is shown that polyhedral cells are better suited for FV schemes [42]. Mesh independence was achieved with 510k cells, seen in figure 3.6. Mass flow rates are assigned to the inlets and pressure profiles at the outlets. A more detailed description of the boundary conditions is presented in section 3.4.

Blood's non-Newtonian behavior is well-documented throughout the literature, however, at high shear rates, the viscosity converges to a constant value mimicking Newtonian characteristics. It can be argued that non-Newtonian effects are negligible in pediatric blood flow simulations, but for completeness the Carreau-Yasuda model was used. It is described as

$$\mu(\dot{\gamma}) = \mu_\infty + (\mu_0 - \mu_\infty)(1 + (\lambda\dot{\gamma})^a)^{(n-1)/a} \tag{3.6}$$

where $\dot{\gamma}$ is the shear rate, μ_∞ is the infinity-shear viscosity (if the fluid were to be treated as Newtonian), μ_0 is the zero-shear viscosity, n is the power constant, λ is the relaxation time constant, and a is the parameter to control shear-thinning.

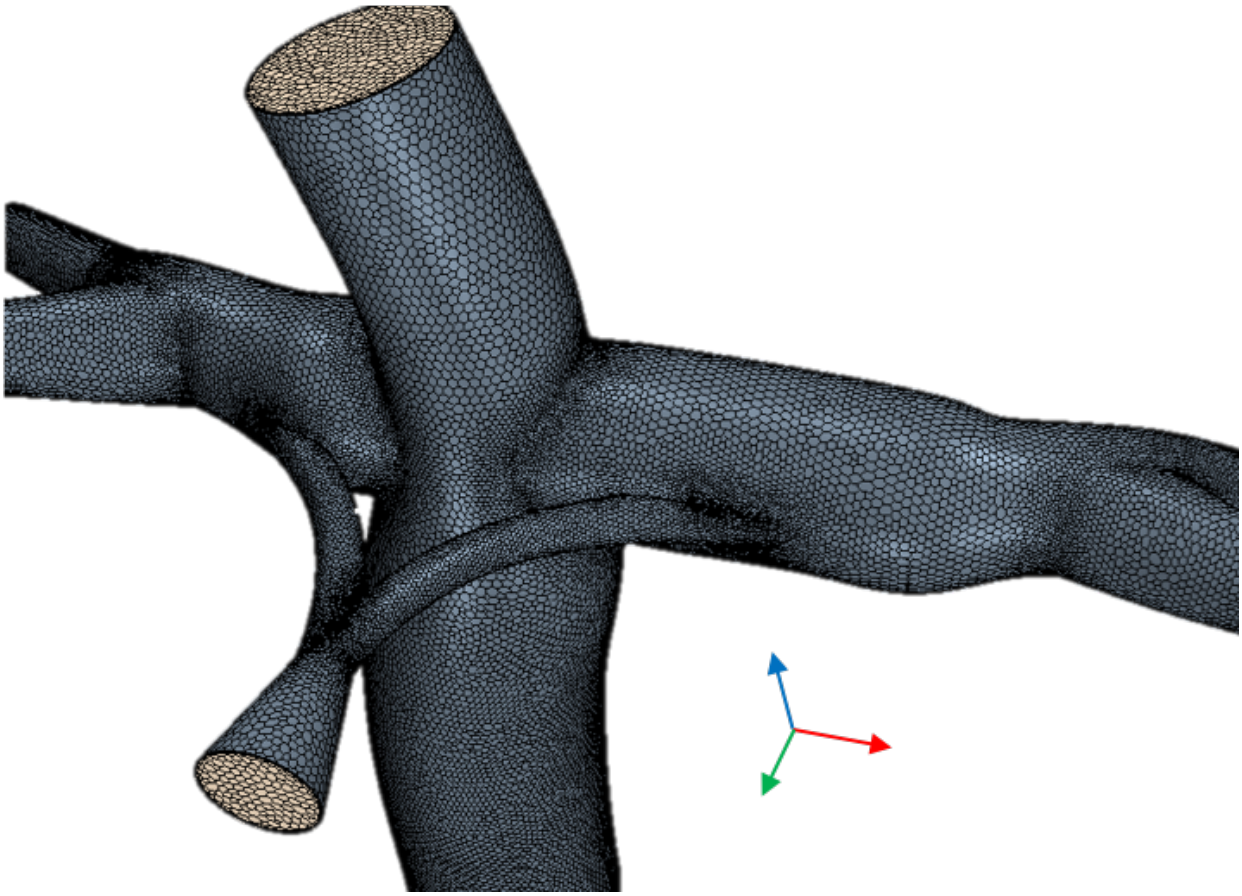

Figure 3.6: Computational mesh of the fluid domain

Note: when $a = 2$, the original Carreau model is obtained. Data points were collected and curve-fitted to obtain the parameter values as shown in table 3.1.

Table 3.1: Carreau-Yasuda Viscosity Model Parameters

μ_∞ (cP)	μ_0 (cP)	λ (s)	n	a
4.000	8.425	0.310	0.333	2.000

3.3.2 Solid Domain: Fluid-Structure Interaction

The main objective of this study was to model the effect of arterial compliance on the self-powered Fontan. Thus, the vessel wall was modeled to be compliant and as such, a FSI model is needed.

This was also done in STAR-CCM+ using a FV approach using polyhedral cells for the same reason as outlined in section 3.3.1. Mesh independence was also achieved with 220k cells. Care was taken to have at least 3 cells in the radial direction as per recommendation by the FSI solver.

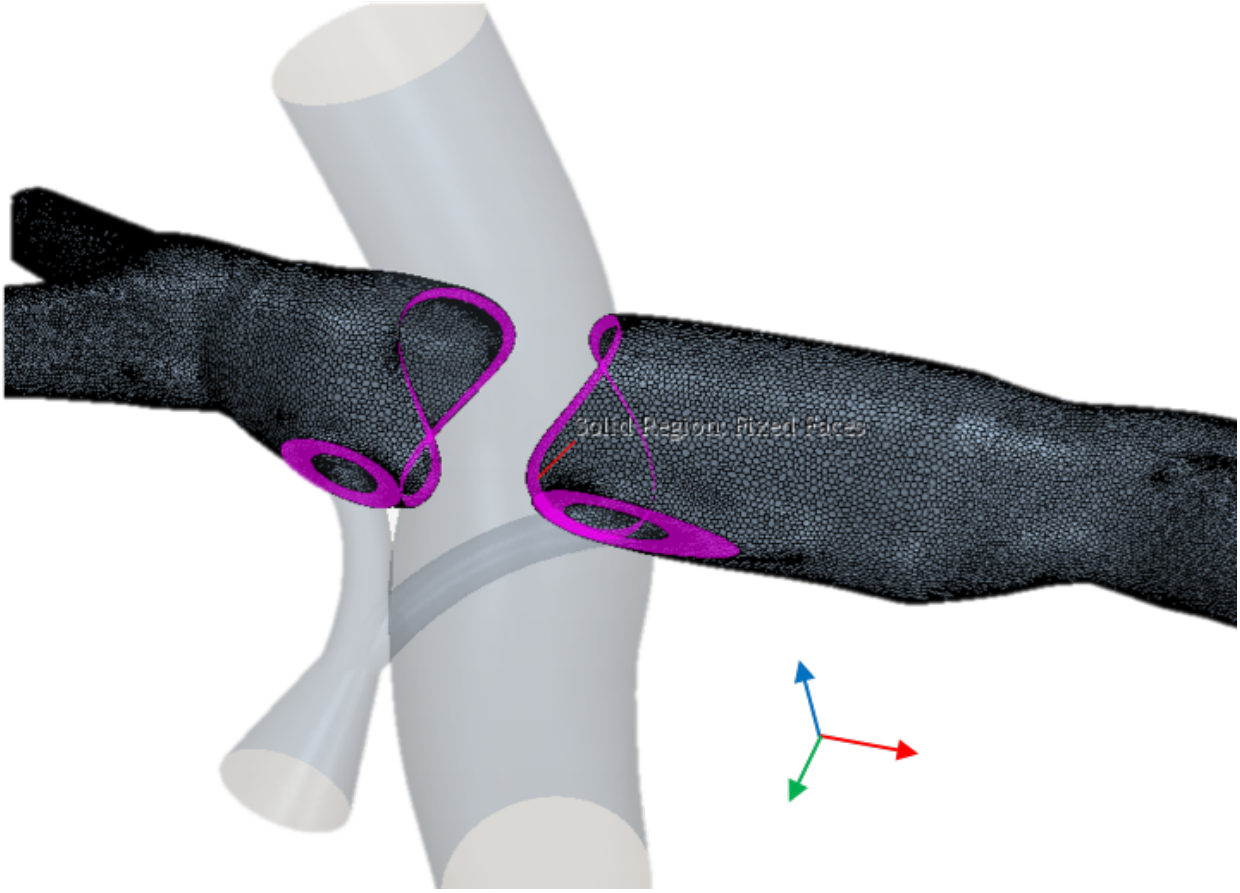

Figure 3.7: Computational mesh of the solid domain

Prescription of the boundary conditions for the solid model are just as important a consideration as the fluid model when vessel wall deformation is important. The IVC segment that connects to the TCPC in the Fontan is a graft as the native IVC terminates much inferior. About the first 50mm below the TCPC consists of graft material. Typically, it is a Gore-Tex graft where the Young's Modulus is several magnitudes higher than the surrounding vessels in the domain of interest. As such, it was assumed to be rigid and only the pulmonary arteries were modeled as compliant, using a Young's Modulus of $E = 0.26MPa$ [25]. The surfaces connected to the TCPC were fixed

(highlighted in pink in figure 3.7) and the rest of the domain was let free.

3.4 0D-3D Tightly-Coupled Scheme

As has been touched on previously in section, hemodynamic simulations are sensitive to the boundary conditions prescribed. The cardiovascular system adapts dynamically to various signals such as arterial/venous pressure, Wall Shear Stress (WSS), and O_2 delivery. These adaptations include vasodilation/vasoconstriction (widening/narrowing of vessel walls), changes in Heart Rate (HR), and changes in venous compliance. If the cardiovascular system attempting to be modeled is assumed to be in a steady-state condition, i.e. the patient is at rest and not moving, then the pressure and volume flow waveforms will be periodically-steady. If you were to overlay the waveforms for each heart cycle, they would match.

These simulations require not only boundary conditions which influence the final solution, but initial conditions - essentially a guess of the initial state of the system. Following the periodically-steady assumption, the initial guess does not have an influence on the final solution. *However*, as the CFD model converges the effective boundary conditions will change. That is, the LPM must adapt to the computed values of the 3D domain and update the boundary conditions which will effect the 3D domain and so on. This is a coupled system and must be modeled as such to achieve physiologically-accurate solutions.

A novel tightly-coupled scheme was developed by Ni [31] and used in this simulation. A Java code is interfaced with STAR-CCM+ and an in-house C++ code to solve the set of ODEs governing the LPM (equations are in Appendix A). First, both the CFD and LPM are initialized. This is an especially important step when performing FSI as the pressures tend to oscillate wildly and diverge if not. The next step is to predict the unknowns of the CFD and then advance one time step. Next,

time is frozen and the CFD and LPM iterate between each other until convergence between the values produced by both are within a certain tolerance. This is done for each time step until the end of the cycle. once cycle-to-cycle convergence is met, the simulation is stopped. This procedure is shown in a flowchart in figure 3.9. The LPM solves for mass flows at the inlets and pressures at the outlets, while the CFD uses those as inputs and solves for pressures at the inlets and mass flows at the outlets.

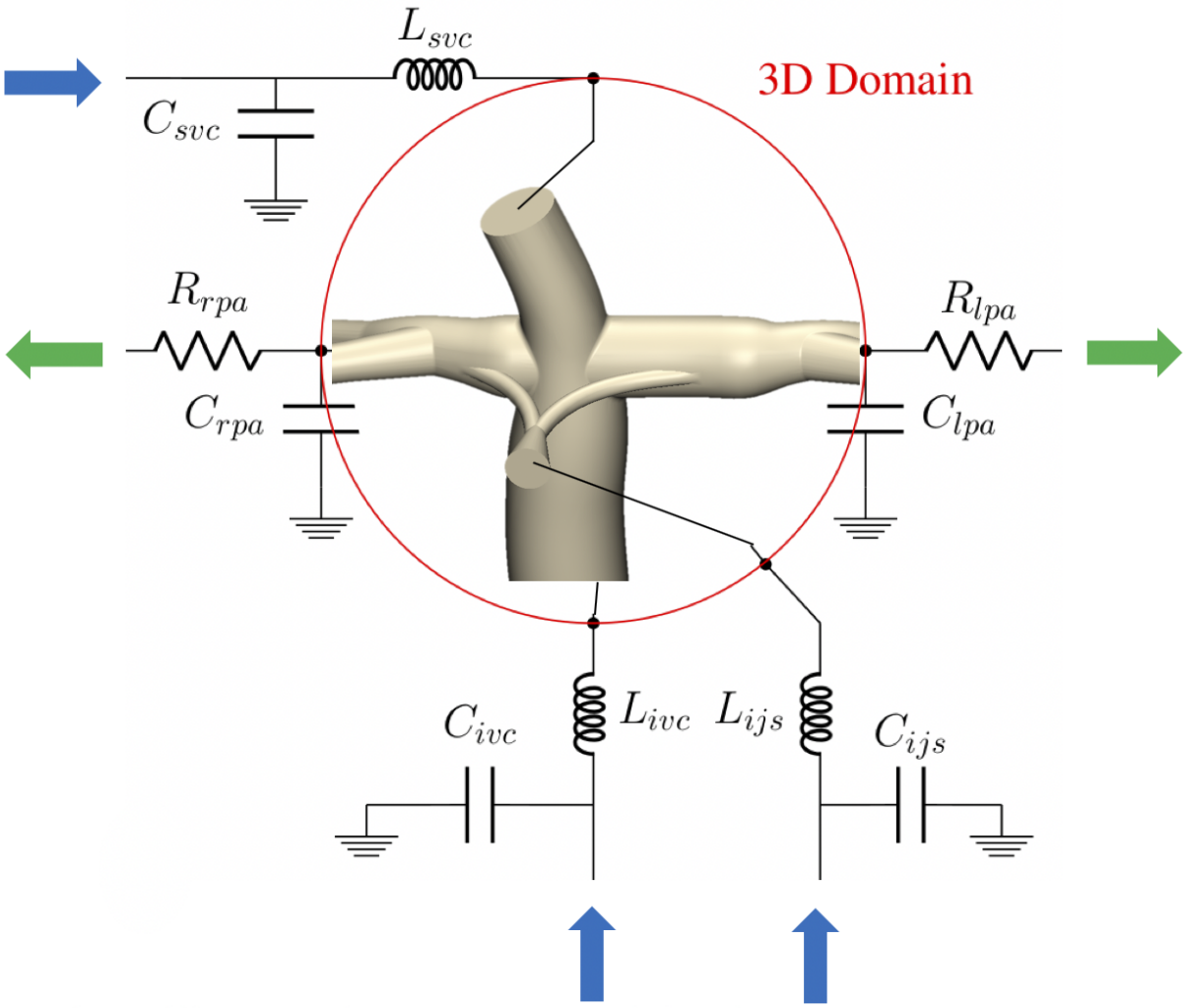

Figure 3.8: Representation of the 3D-0D coupling. Closeup image of the 3D domain area

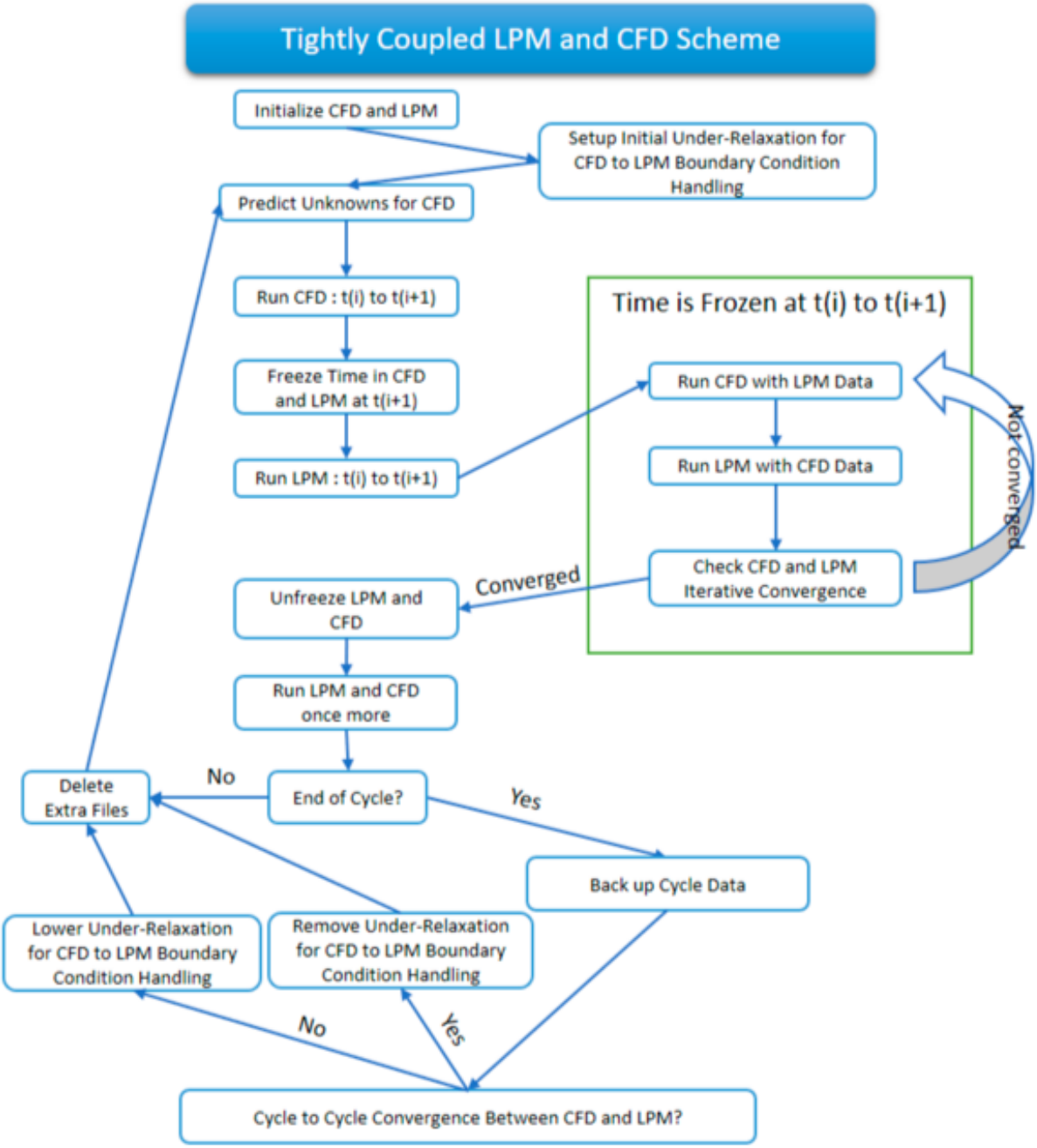

Figure 3.9: Flowchart of the tightly-coupled scheme used. Taken from Ni [31]

CHAPTER 4: RESULTS

Four different cases were run: IJS off, IJS on with baseline PVR, IJS on with -40% PVR, and IJS on with -60% PVR. The PVR was varied to explore the effects of PVR on IJS performance as the pulmonary volume flow/PVR relationship is not well known. The results are listed in table 4.1. Aligning with our expectations, IVC pressure decreased, CO increased, systemic O_2 delivery increased, and there was more pulsatility in the pulmonary arteries, except for the IJS on, nominal PVR case. These trends are plotted in figure 4.1.

Table 4.1: Time-averaged hemodynamic quantities of interest: Q_P/Q_S is the ratio of pulmonary to systemic volume flow, PP is the pulse pressure in the pulmonary arteries, Q_{SYS} is the systemic volume flow rate, Q_{IJS} is the IJS volume flow rate, and CO is the Cardiac Output

IJS Status	PVR	IVC Pressure (mmHg)	Δp	Q_P/Q_S	PP (mmHg)	Systemic O_2 Delivery (L O_2 / min)	Q_{SYS} (L/min)	Q_{IJS} (L/min)	CO (L/min)
OFF	Nominal	16.520	—	1.003	3.329	0.137	1.109	0.000	1.113
ON	Nominal	18.820	+2.300	1.479	3.891	0.128	0.915	0.439	1.355
ON	-40%	16.140	-0.380	1.475	5.411	0.159	1.064	0.505	1.570
ON	-60%	14.110	-2.410	1.478	7.657	0.174	1.137	0.543	1.682

A similar study was carried out in our group with the assumption of rigid walls [32]. Surprisingly, the FSI study had adverse effects - dropping IVC pressure by 2.41 mmHg compared to 2.88 mmHg for the rigid study. If we consider the cross-sectional area change involved with deformation of the vessel wall, it starts to become clear why this is. It was assumed that FSI would help the jet effect as there would be more volume in the pulmonary arteries as they expanded for the extra mass emanating from the IJS to diffuse. This aspect of the 'jet effect' is important as the concept was borrowed from the oil and gas industry where the streams are typically pumped to an exit facing atmospheric conditions. It was overlooked that the IJS would reduce the internal pressure (thus the transmural pressure) which is what pushes the vessel wall to expand. Lower pressures indicate smaller cross-sectional areas and *higher* resistances. A plot of the cross-sectional area of the RPA

outlet for each case is in figure 4.2. The LPA plot was left out because they are almost identicalas an even right to left pulmonary flow split is assumed. If we compute the effective resistance using equation 3.2 and the difference in these resistances from the baseline model, we can estimate how much of an effect the area reduction is for estimating IVC pressure drops (table 4.2).

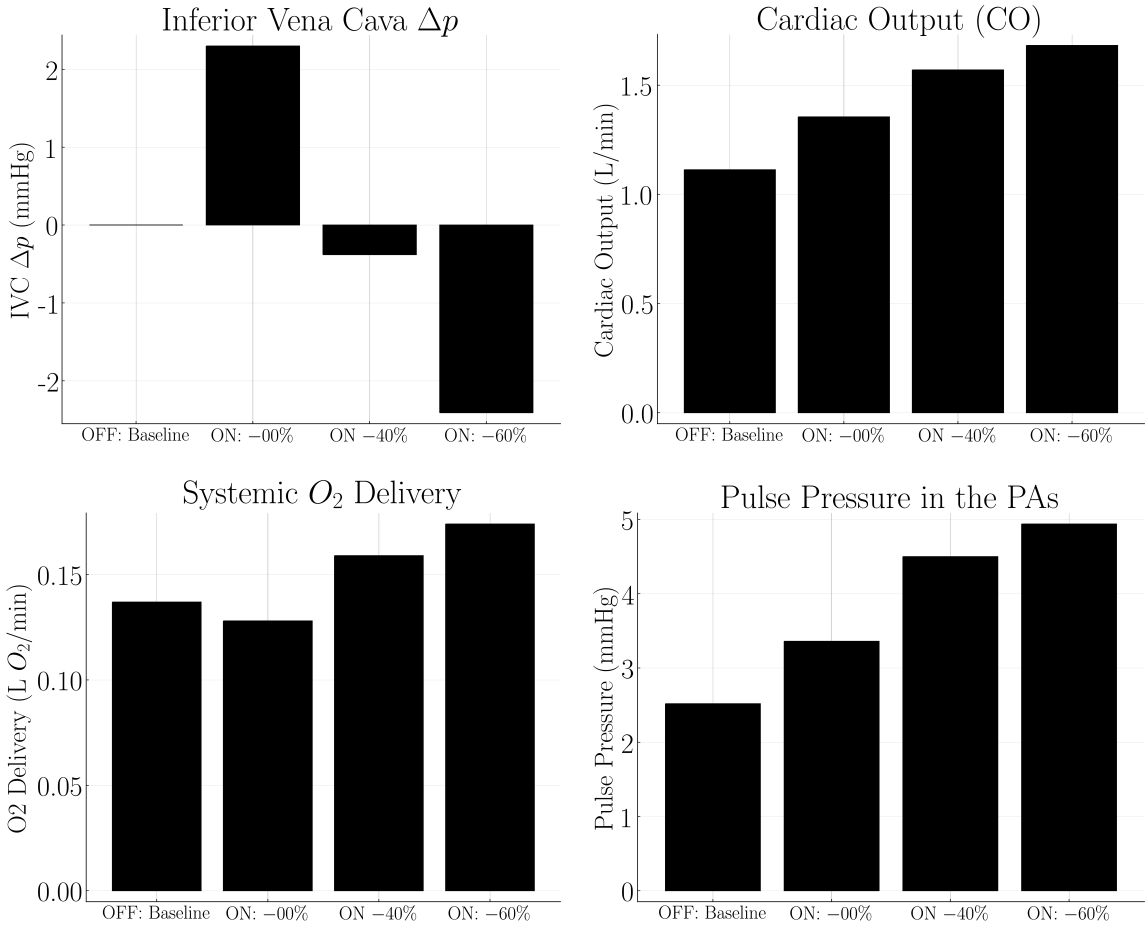

Figure 4.1: Hemodynamic parameters of interest as PVR is dropped

The resistances calculated are on a per unit length basis, so adjusting for length and calculating for the amount of flow through the pulmonary arteries using

$$\Delta p = Q_{RPA}/4(R_{on,-60\%}10)$$

we get about 0.96 mmHg added to the predicted pressure because of the reduction in area change. If you were to factor this in, it would constitute an even better pressure drop than the rigid study.

Table 4.2: Comparing resistances

IJS Status	PVR Drop	Average Area (mm^2)	Resistance, R (mmHg s / mL mm)	ΔR
OFF	Nominal	44.142	0.387	—
ON	Nominal	44.984	0.372	-0.015
ON	-40%	44.040	0.389	0.002
ON	-60%	43.437	0.400	0.013

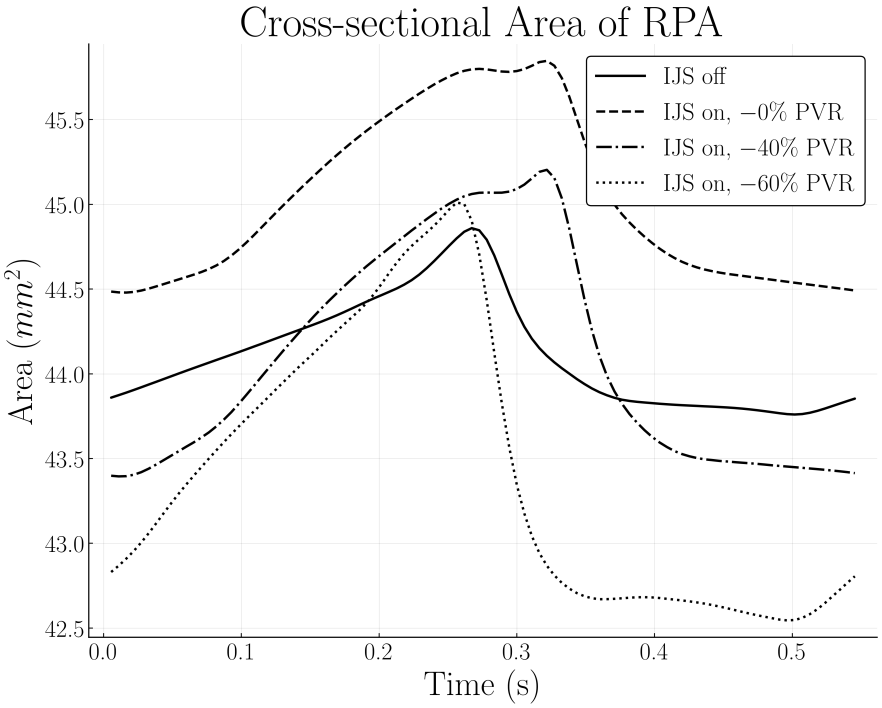

Figure 4.2: RPA outlet area

The answer to this discrepancy lies in this only other difference in the model - the IJS is anastomosed to the artery wall, unlike the rigid version where the jet cuts into the main flow and is ejected into the centerline of the ambient flow. Although the jet at the wall does not maximize entrainment because it is not parallel to the ambient flow, the IJS graft itself does not block the flow like a

cylinder in cross flow. Looking at the velocity vector scene from a superior view (figure 4.3), we see the competing forces of the jet and ambient flow in the form of oscillations of the jet direction. This is most notable if you compare the late systole (figure 4.3b) and late diastole (figure 4.3d).

It is useful to calculate pressure-volume loops for the RV as a quick qualitative (although many quantitative measures can be extracted as well) check of the hearts performance. A plot of each cases PV loop can be seen in figure 4.4. When the IJS is turned on but PVR is left unchanged, there is a reduction in ventricle performance. Once PVR is dropped, and thus the afterload on the heart, the PV loop moves in the northwest direction indicating an improvement in cardiac function. This behavior aligns with the trend of the CO which is expected as the two quantities are related.

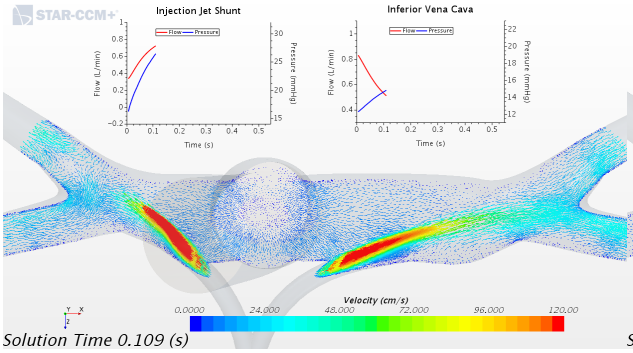

(a) Early systole

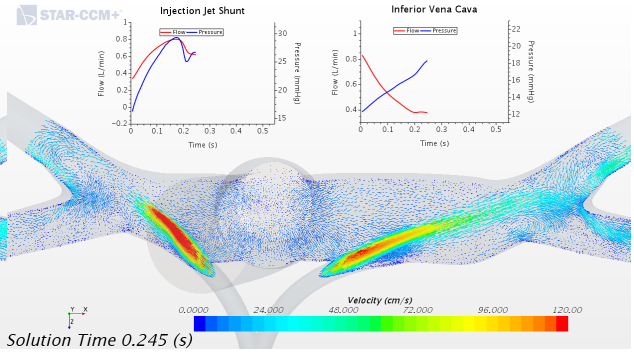

(b) Late systole

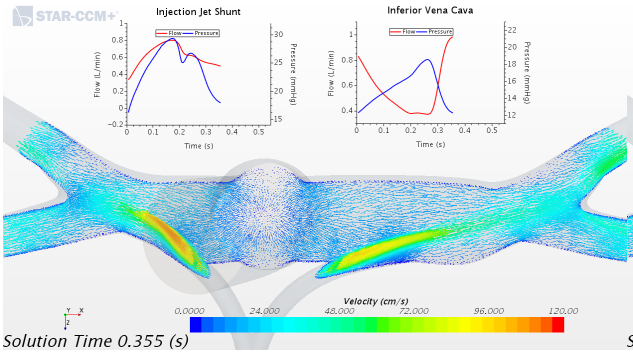

(c) Early diastole

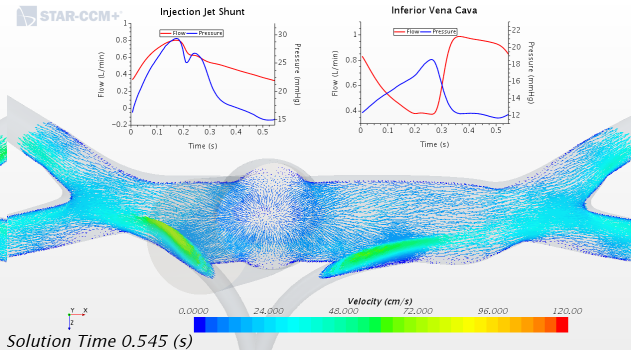

(d) Late diastole

Figure 4.3: Superior view of IJS on, -60% PVR case

The volume in the RV can be calculated as

$$V(t) = \frac{P(t)}{E(t)} + V_d \tag{4.1}$$

where $E(t)$ is the elastance function (eq. 3.5) and V_d is the diastolic volume [43].

Exploring the qualitative results in more detail oftentimes bring useful insights to improving the local hemodynamic parameters such as IJS size, shape, sites of anastomosis, etc. Zooming in on figure 4.5 (RPA, or left side of figure), there are vortices that form in the flow much like those generated from the wing tip of an airplane. These contribute to a loss in effective momentum transfer from the jet to ambient flow. Typically, these jets are incorporated into a Converging-Diverging (CD) nozzle with the half-angles of the diverging section carefully chosen to avoid boundary layer separation and thus re-circulation zones where losses are incurred.

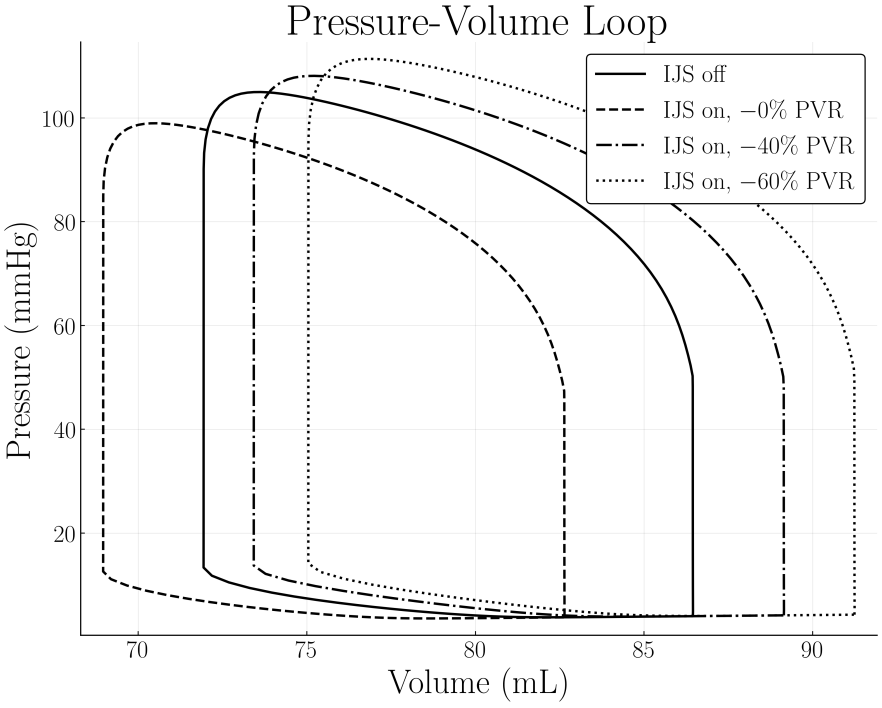

Figure 4.4: Pressure-volume loops of the RV for each case run

Taking a look at the velocity magnitudes down the RPA branch vessels reveals an abnormal ve-

locity distribution at the bifurcation (figure 4.6). The jet is re-directed to the anterior branch of the pulmonary arteries and can lead to uneven flow splits which is less efficient for the lungs to oxygenate the blood. This drawback is offset by increased O_2 delivery with the augmentation of the IJS flow.

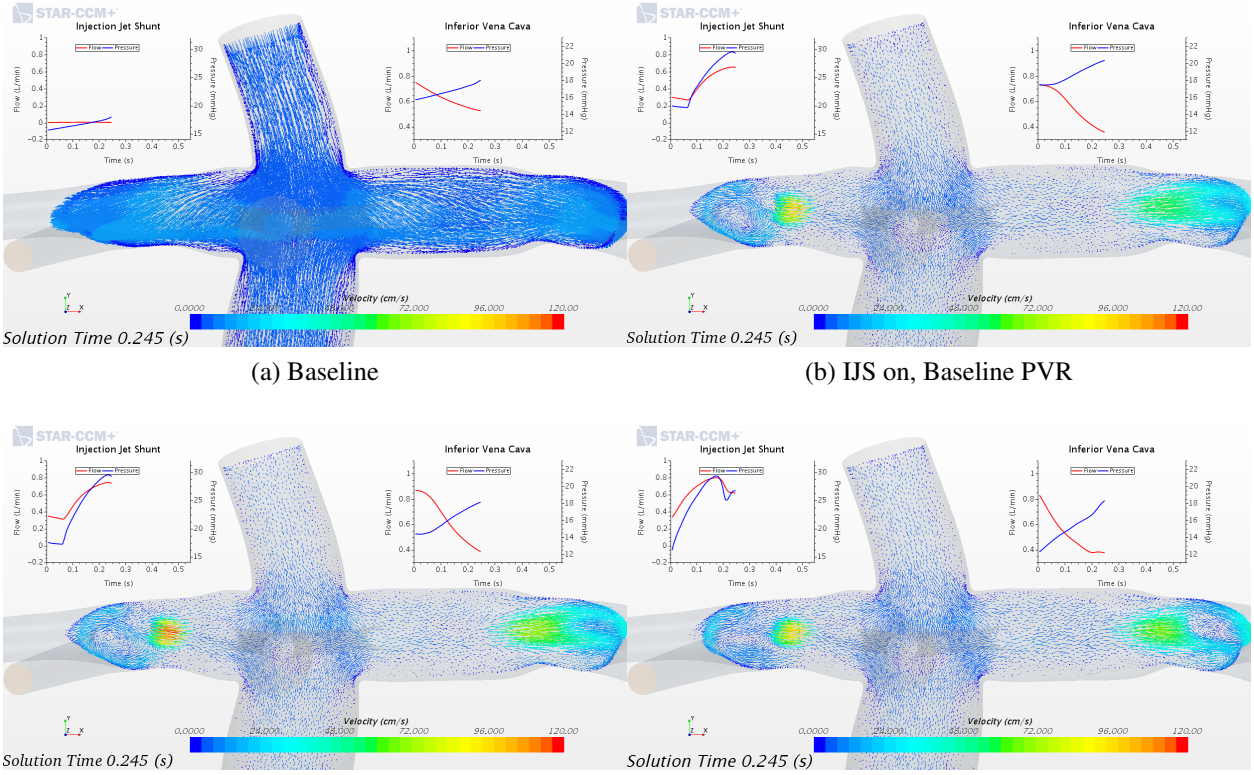

(a) Baseline

(b) IJS on, Baseline PVR

(c) IJS on, -40% PVR

(d) IJS on, -60% PVR

Figure 4.5: Posterior view of TCPC during mid systole

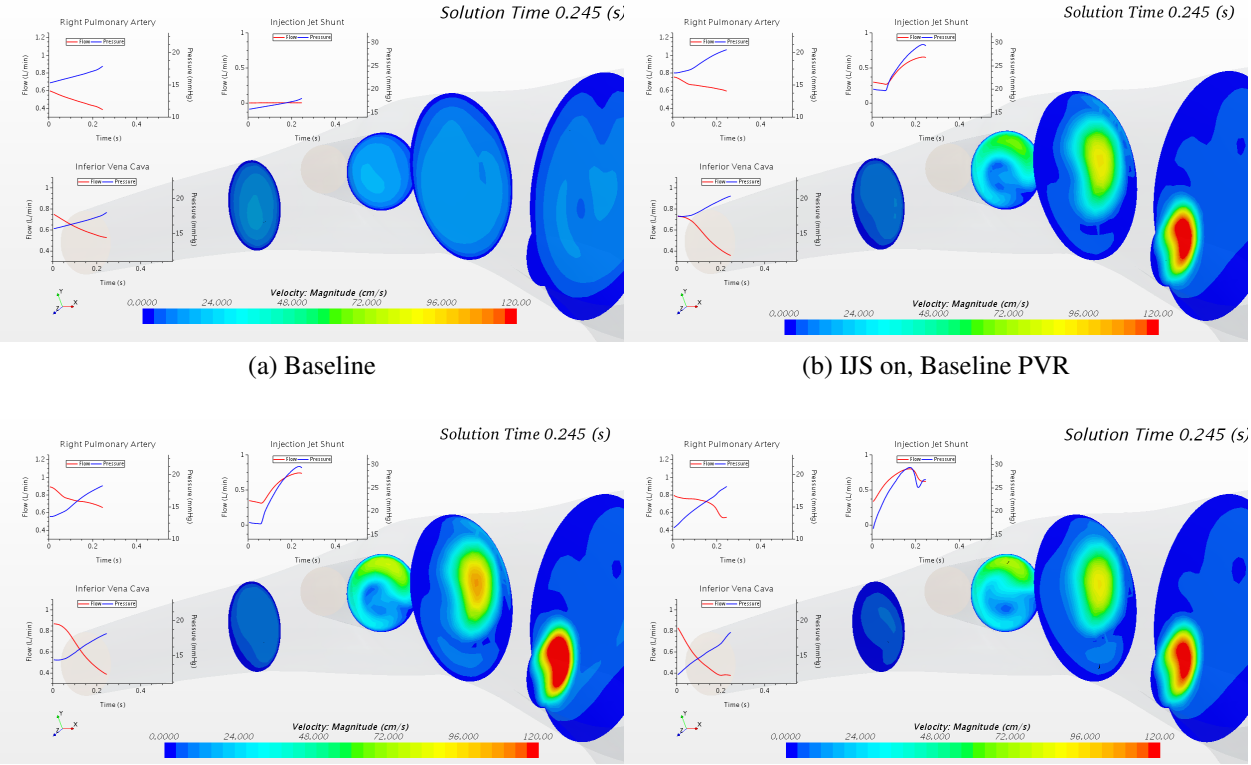

(a) Baseline

(b) IJS on, Baseline PVR

(c) IJS on, -40% PVR

(d) IJS on, -60% PVR

Figure 4.6: Velocity magnitude of the RPA branch vessels during mid systole

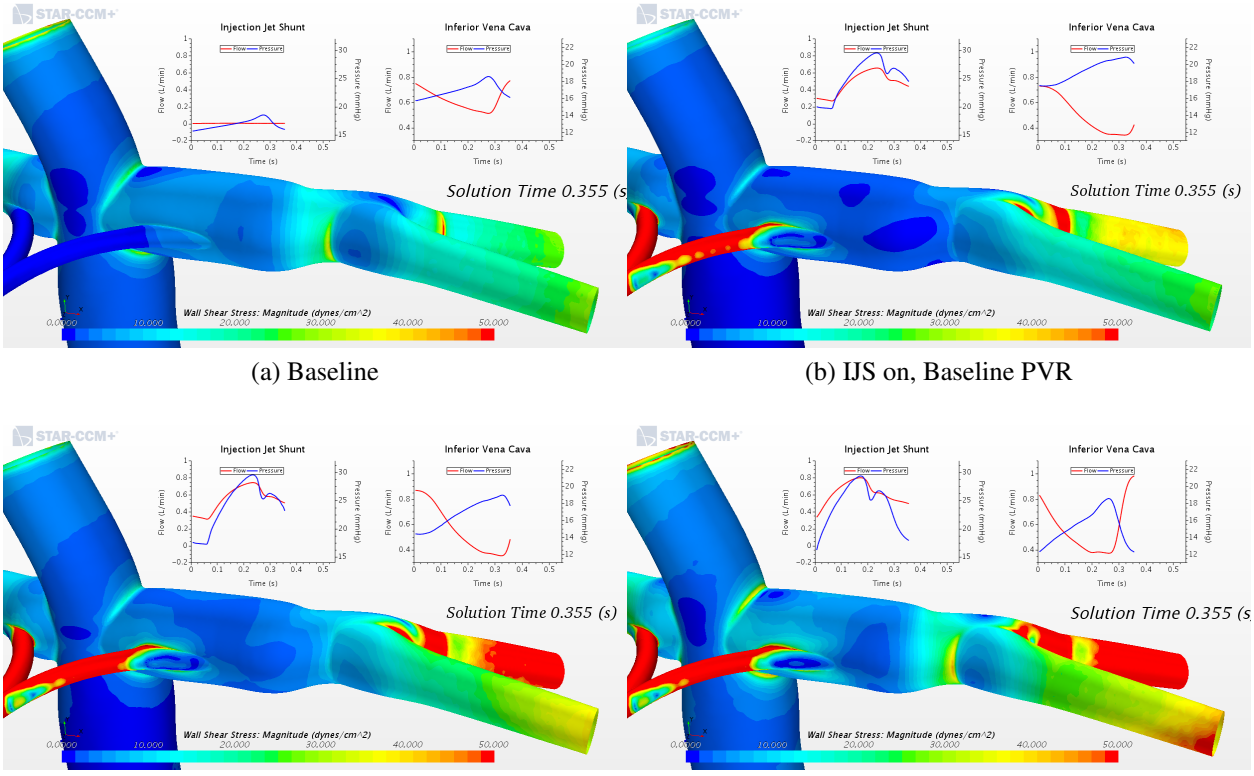

(a) Baseline

(b) IJS on, Baseline PVR

(c) IJS on, -40% PVR

(d) IJS on, -60% PVR

Figure 4.7: Wall Shear Stress during early diastole

CHAPTER 5: CONCLUSION

The IJS concept proved to have opposite results than what was initially expected. Inclusion of FSI into the model does not reduce the IVC pressure as much as the similar rigid wall study due to lower overall transmural pressure in the system. The difference in pressures is small enough to assume inclusion of FSI for Fontan simulations is not necessary. The computational time is significantly increased (about 75%) for minor a change in results. If one were interested in the precise shape of pressure waveforms or the WSS contours, then FSI should be considered. For the purpose of evaluating the 'self-powered' Fontan IJS concept where cycle-averaged IVC pressure is the main concern, a rigid wall assumption is suitable.

This study further confirms the efficacy of the IJS improving all of the metrics set out to achieve - reduced IVC pressure, increased CO, and increased pulse pressure in the pulmonary arteries. Although the reduction in IVC pressure is not clinically significant, introduction of IJS may still be advantageous because it presents little risk unlike mechanical support devices. For this reason, further designs along this route should be considered.

APPENDIX A: CIRCUIT DIAGRAMS AND EQUATIONS

The coupled set of Ordinary Differential Equations (ODE) that govern the closed-loop circuit for initialization of the IJS injecting into the pulmonary arteries with FSI is as follows

$$\frac{d}{dt}(p_{ra}) = \frac{1}{C_{ra}}\Big(I_{in} - \frac{p_{ra} - p_{rv}}{R_{tric}}H(t)\Big) \tag{A.1}$$

$$\frac{d}{dt}(p_{rv}) = \frac{1}{C_{ra}(t)}\Big(\frac{p_{ra} - p_{rv}}{R_{tric}}H(t) - p_{rv}\frac{d}{dt}(C_{rv}(t)) - \frac{p_{rv} - p_{ao}}{R_{pv}}H(t)\Big) \tag{A.2}$$

$$\frac{d}{dt}(p_{ao}) = \frac{1}{C_{ao}}\Big(\frac{p_{rv} - p_{ao}}{R_{pv}}H(t) - \frac{p_{ao} - p_{ijs}}{R_G} - Q_{ao}\Big) \tag{A.3}$$

$$\frac{d}{dt}(Q_{ao}) = \frac{1}{L_{ao}}(p_{ao} - Q_{ao}R_{ao} - p_{split}) \tag{A.4}$$

$$\frac{d}{dt}(p_{lbab}) = \frac{1}{C_{lbab}}\Big(\frac{p_{split} - p_{lbab}}{R_{da}} - Q_{lbab}\Big) \tag{A.5}$$

$$\frac{d}{dt}(Q_{lbab}) = \frac{1}{L_{lbab}}(p_{lbab} - Q_{lbab}R_{lbab} - p_{lbvb}) \tag{A.6}$$

$$\frac{d}{dt}(p_{lbvb}) = \frac{1}{C_{lbvb}}\Big(Q_{lbab} - \frac{p_{lbvb} - p_{ivc}}{R_{lbvb}}\Big) \tag{A.7}$$

$$\frac{d}{dt}(p_{corab}) = \frac{1}{C_{corab}}\Big(\frac{p_{split} - p_{corab}}{R_{cor}} - \frac{p_{corab} - p_{corvb}}{R_{corab}}\Big) \tag{A.8}$$

$$\frac{d}{dt}(p_{corvb}) = \frac{1}{C_{corvb}}\Big(\frac{p_{corab} - p_{corvb}}{R_{corab}} - \frac{p_{corvb} - p_{ra}}{R_{corvb}(t)}\Big) \tag{A.9}$$

$$\frac{d}{dt}(p_{subab}) = \frac{1}{C_{sob}}\Big(\frac{p_{split} - p_{subab}}{R_{sub}} - Q_{subab}\Big) \tag{A.10}$$

$$\frac{d}{dt}(Q_{subab}) = \frac{1}{L_{sob}}\Big(p_{subab} - Q_{subab}R_{sob} - p_{subvb}\Big) \tag{A.11}$$

$$\frac{d}{dt}(p_{subvb}) = \frac{1}{C_{dsb}}\Big(Q_{subab} - \frac{p_{subvb} - p_{svc}}{R_{dsb}}\Big) \tag{A.12}$$

$$\frac{d}{dt}(p_{carab}) = \frac{1}{C_{cob}}\Big(\frac{p_{split} - p_{carab}}{R_{car}} - Q_{carab}\Big) \tag{A.13}$$

$$\frac{d}{dt}(Q_{carab}) = \frac{1}{L_{cob}}\Big(p_{carab} - Q_{carab}R_{cob} - p_{carvb}\Big) \tag{A.14}$$

$$\frac{d}{dt}(p_{carvb}) = \frac{1}{C_{dcb}}\Big(Q_{carab} - \frac{p_{carvb} - p_{svc}}{R_{dcb}}\Big) \tag{A.15}$$

$$\frac{d}{dt}(p_{rlung}) = \frac{1}{C_{rlung}}\Big(\frac{p_{cfd-rpa} - p_{rlung}}{R_{rpa}} - Q_{rlung}\Big) \tag{A.16}$$

$$\frac{d}{dt}(Q_{rlung}) = \frac{1}{L_{rlung}}\Big(p_{rlung} - Q_{rlung}R_{rlung} - p_{rpvb}\Big) \tag{A.17}$$

$$\frac{d}{dt}(p_{rpvb}) = \frac{1}{C_{rpvb}}\Big(Q_{rlung} - \frac{p_{rpvb} - p_{ra}}{R_{rpvb}}\Big) \tag{A.18}$$

$$\frac{d}{dt}(p_{llung}) = \frac{1}{C_{llung}}\Big(\frac{p_{cfd-lpa} - p_{llung}}{R_{lpa}} - Q_{llung}\Big) \tag{A.19}$$

$$\frac{d}{dt}(Q_{llung}) = \frac{1}{L_{llung}}\Big(p_{llung} - Q_{llung}R_{llung} - p_{lpvb}\Big) \tag{A.20}$$

$$\frac{d}{dt}(p_{lpvb}) = \frac{1}{C_{lpvb}}\Big(Q_{llung} - \frac{p_{lpvb} - p_{ra}}{R_{lpvb}}\Big) \tag{A.21}$$

$$\frac{d}{dt}(p_{cfd-rpa}) = \frac{1}{C_{rpa}}\Big(\frac{p_{tcpc} - p_{cfd-rpa}}{R_{cfd-rpa}} - \frac{p_{cfd-rpa} - p_{rlung}}{R_{rpa}}\Big) \tag{A.22}$$

$$\frac{d}{dt}(p_{cfd-lpa}) = \frac{1}{C_{lpa}}\Big(\frac{p_{tcpc} - p_{cfd-lpa}}{R_{cfd-lpa}} - \frac{p_{cfd-lpa} - p_{llung}}{R_{lpa}}\Big) \tag{A.23}$$

$$\frac{d}{dt}(p_{ivc}) = \frac{1}{C_{ivc}}\Big(\frac{p_{lbvb} - p_{ivc}}{R_{lbvb}} - Q_{ivc}\Big) \tag{A.24}$$

$$\frac{d}{dt}(Q_{ivc}) = \frac{1}{L_{ivc}}\Big(p_{ivc} - Q_{ivc}R_{cfd-ivc} - p_{tcpc}\Big) \tag{A.25}$$

$$\frac{d}{dt}(p_{svc}) = \frac{1}{C_{svc}}\Big(\frac{p_{subvb} - p_{svc}}{R_{dsb}} - \frac{p_{carvb} - p_{svc}}{R_{dcb}}\Big) \tag{A.26}$$

$$\frac{d}{dt}(Q_{svc}) = \frac{1}{L_{svc}}\Big(p_{svc} - Q_{svc}R_{cfd-svc} - p_{tcpc}\Big) \tag{A.27}$$

$$\frac{d}{dt}(p_{ijs}) = \frac{1}{C_G}\Big(\frac{p_{tcpc} - p_{ijs}}{R_G} - Q_{ijs}\Big) \tag{A.28}$$

$$\frac{d}{dt}(Q_{ijs}) = \frac{1}{L_G}\Big(p_{ijs} - Q_{ijs}R_{cfd-ijs} - p_{tcpc}\Big) \tag{A.29}$$

$$\frac{d}{dt}(p_{tcpc}) = \frac{1}{C_{tcpc}}\Big(Q_{ijs} + Q_{ivc} + Q_{svc} + \frac{p_{tcpc} - p_{cfd-lpa}}{R_{cfd-lpa}} + \frac{p_{tcpc} - p_{cfd-rpa}}{R_{cfd-rpa}}\Big) \tag{A.30}$$

where I_{in} and p_{split} are defined as follows

$$I_{in} = \frac{p_{rpvb} - p_{ra}}{R_{rpvb}} + \frac{p_{lpvb} - p_{ra}}{R_{lpvb}} + \frac{p_{corvb} - p_{ra}}{R_{corvb}}$$

$$p_{split} = \frac{Q_{ao} + p_{lbab}/R_{da} + p_{subab}/R_{sub} + p_{corab}/R_{cora} + p_{carab}/R_{carotid}}{R_{da}^{-1} + R_{sub}^{-1} + R_{cora}^{-1} + R_{carotid}^{-1}}$$

and once the circuit is opened up to be tightly-coupled with the 3D CFD, we replace the ODEs for the following:

$$\frac{d}{dt}(p_{cfd-rpa}) = \frac{1}{C_{rpa}}\Big(Q_{cfd-rpa} - \frac{p_{cfd-rpa} - p_{rlung}}{R_{rpa}}\Big)$$

$$\frac{d}{dt}(p_{cfd-lpa}) = \frac{1}{C_{lpa}}\Big(Q_{cfd-lpa} - \frac{p_{cfd-lpa} - p_{llung}}{R_{lpa}}\Big)$$

$$\frac{d}{dt}(Q_{ivc}) = \frac{1}{L_{ivc}}\Big(p_{ivc} - p_{cfd-ivc}\Big)$$

$$\frac{d}{dt}(Q_{svc}) = \frac{1}{L_{svc}}\Big(p_{svc} - p_{cfd-svc}\Big)$$

$$\frac{d}{dt}(Q_{ijs}) = \frac{1}{L_{ijs}}\Big(p_{ijs} - p_{cfd-ijs}\Big)$$

APPENDIX B: 3D CFD SCENES

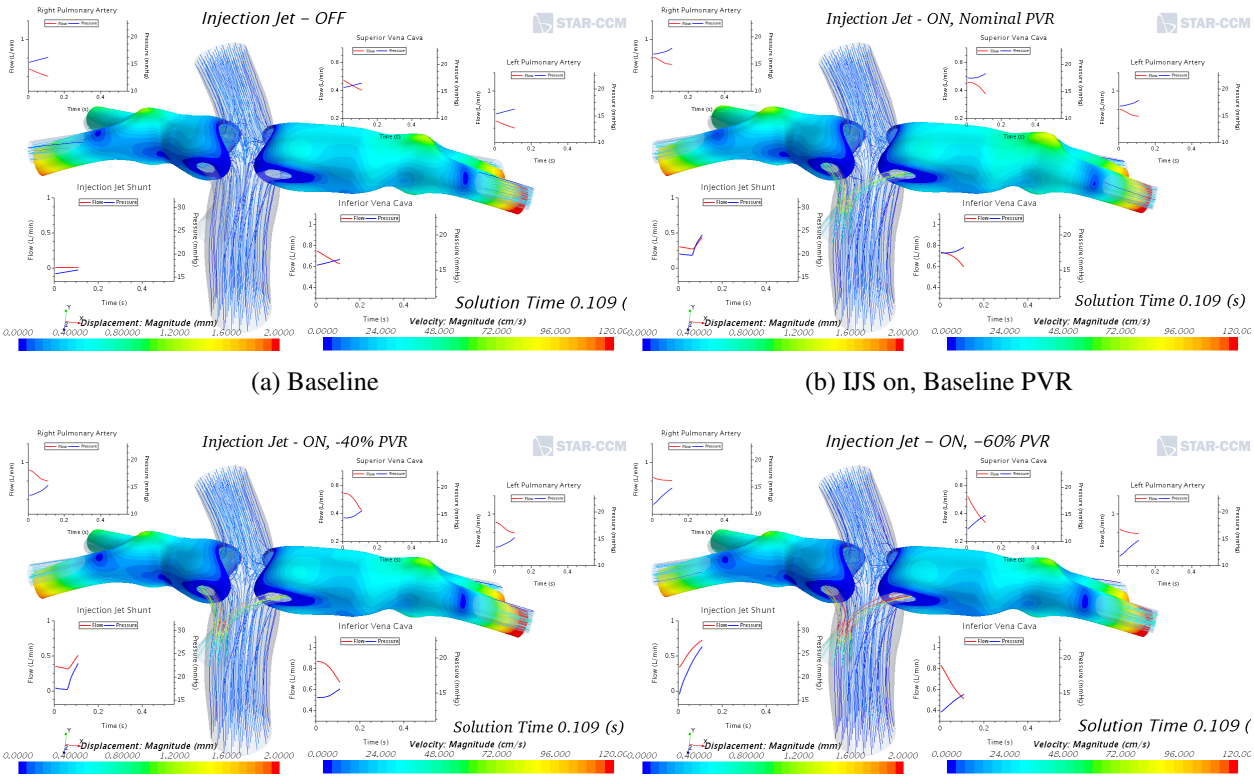

(a) Baseline

(b) IJS on, Baseline PVR

(c) IJS on, -40% PVR

(d) IJS on, -60% PVR

Figure B.1: Displacement and streamlines during early systole - anterior view

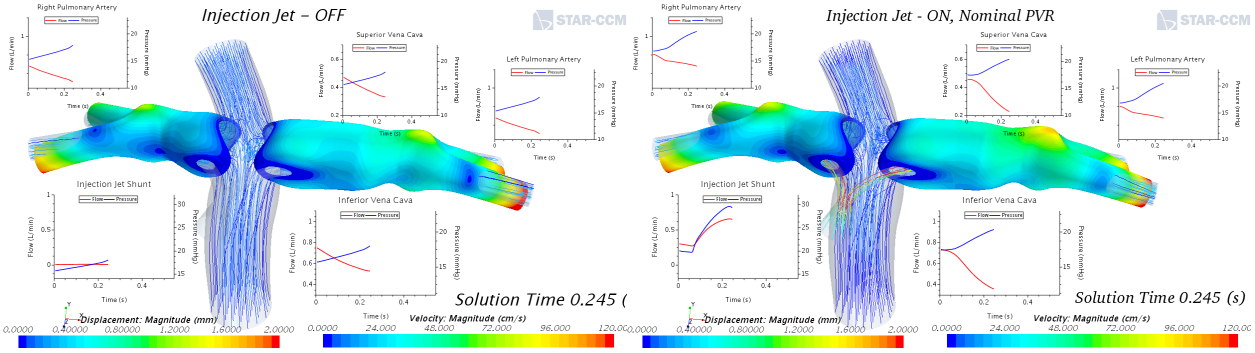

(a) Baseline

(b) IJS on, Baseline PVR

(c) IJS on, -40% PVR

(d) IJS on, -60% PVR

Figure B.2: Displacement and streamlines during late systole - anterior view

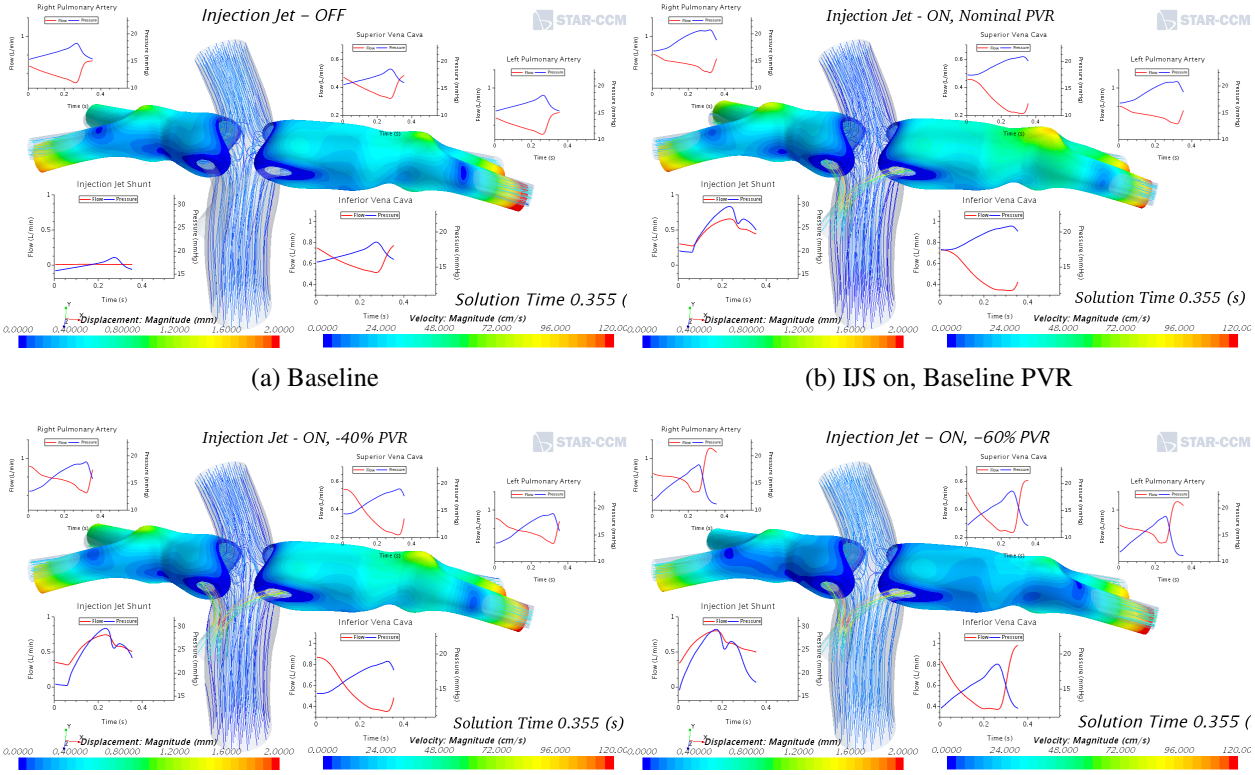

(a) Baseline

(b) IJS on, Baseline PVR

(c) IJS on, -40% PVR

(d) IJS on, -60% PVR

Figure B.3: Displacement and streamlines during early diastole - anterior view

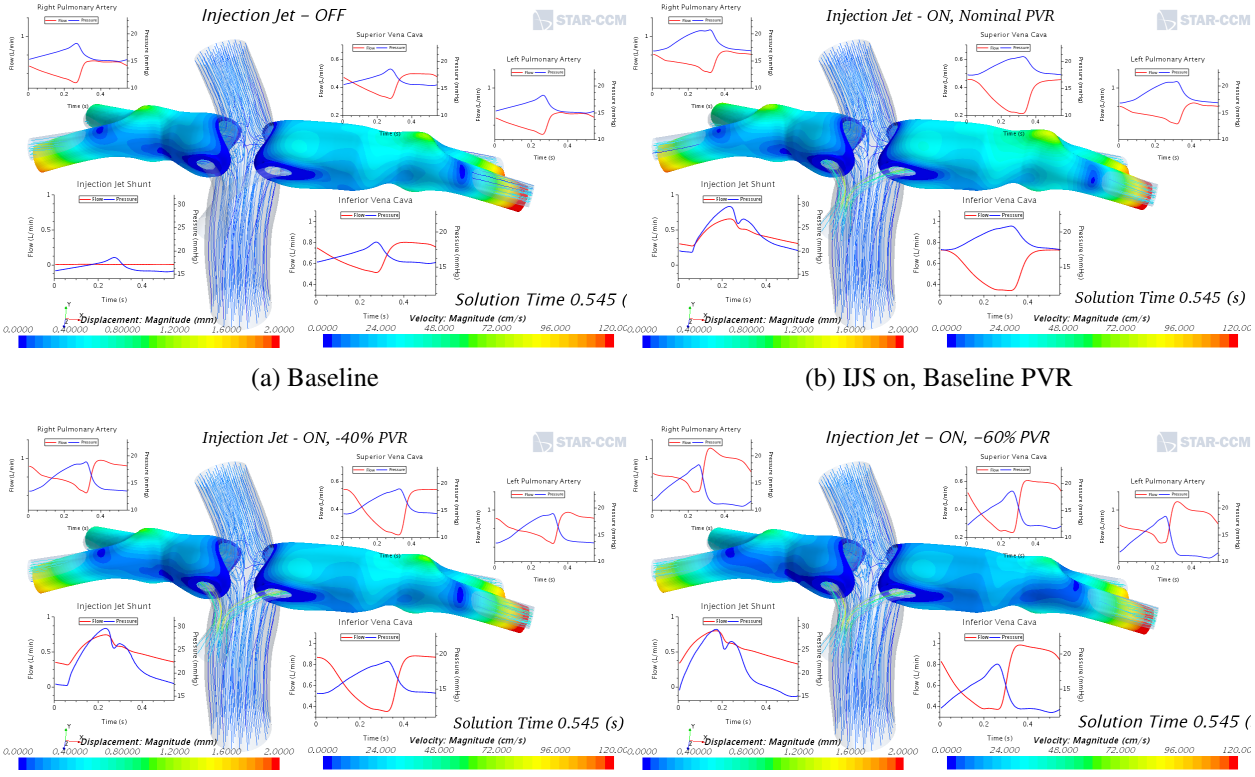

(a) Baseline

(b) IJS on, Baseline PVR

(c) IJS on, -40% PVR

(d) IJS on, -60% PVR

Figure B.4: Displacement and streamlines during late diastole - anterior view

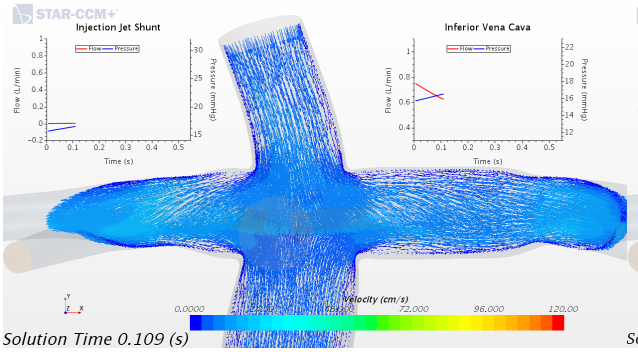

(a) Baseline

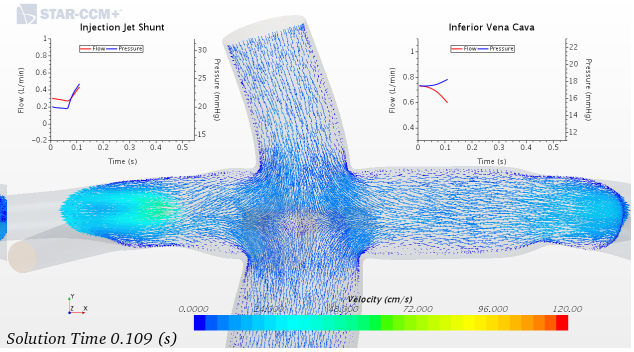

(b) IJS on, Baseline PVR

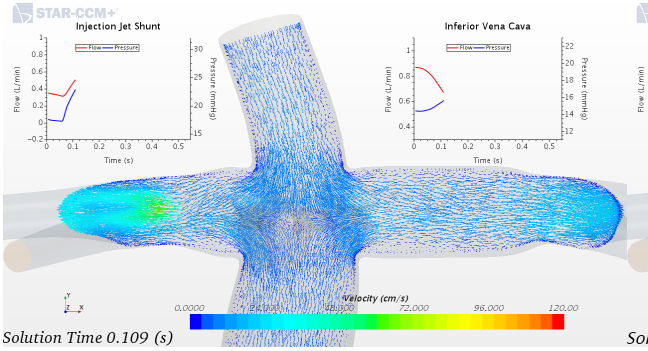

(c) IJS on, -40% PVR

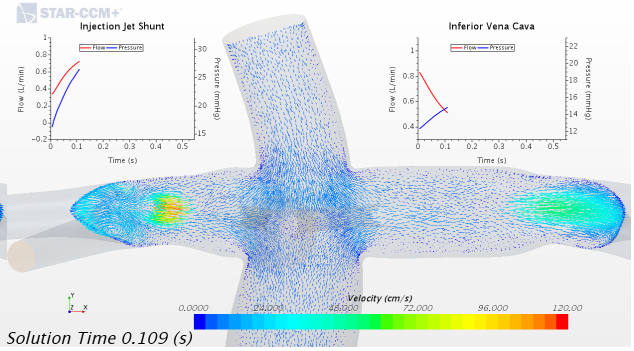

(d) IJS on, -60% PVR

Figure B.5: Velocity vectors during early systole - anterior view

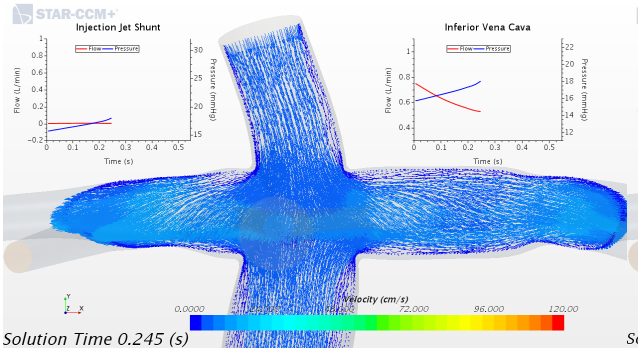

(a) Baseline

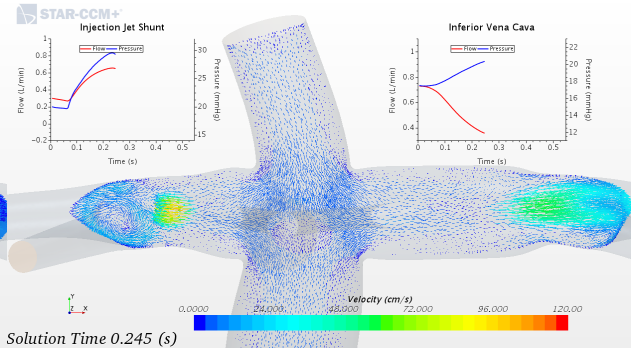

(b) IJS on, Baseline PVR

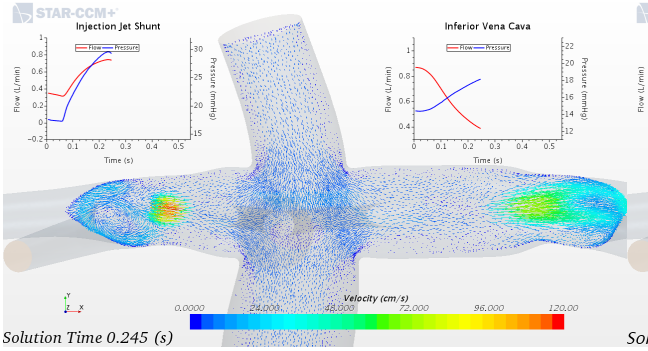

(c) IJS on, -40% PVR

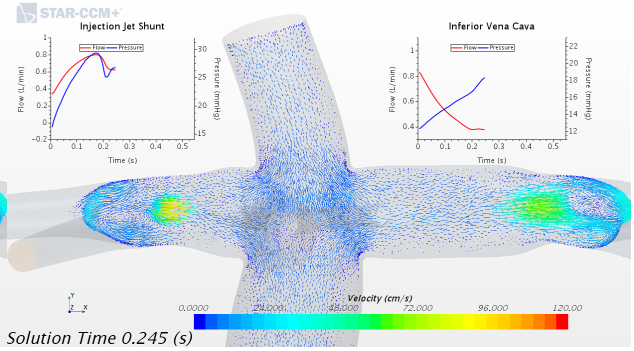

(d) IJS on, -60% PVR

Figure B.6: Velocity vectors during late systole - anterior view

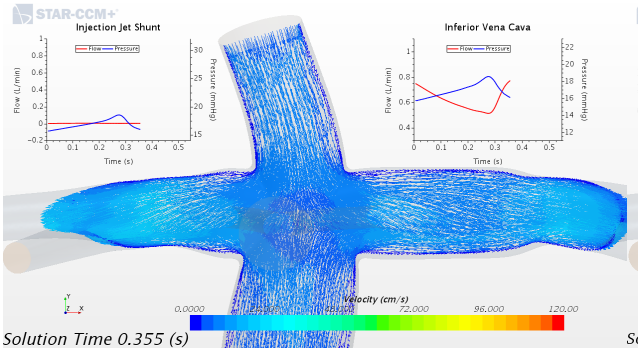

(a) Baseline

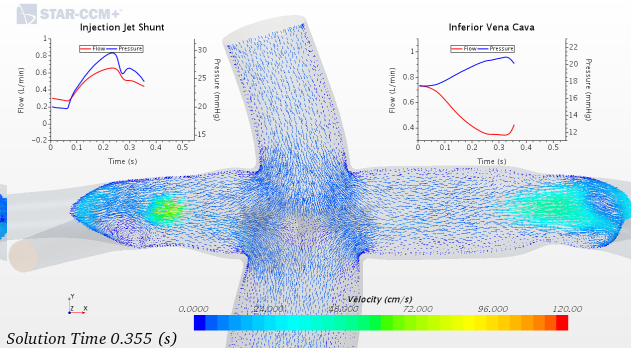

(b) IJS on, Baseline PVR

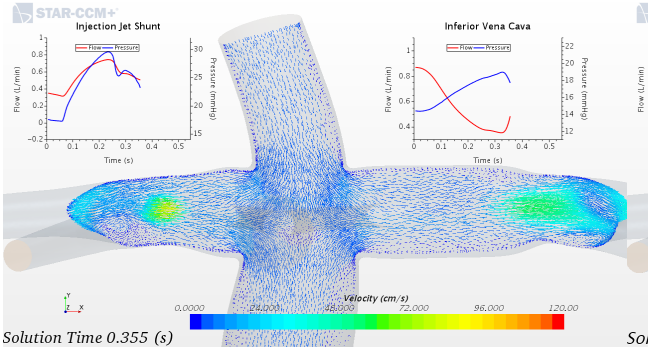

(c) IJS on, -40% PVR

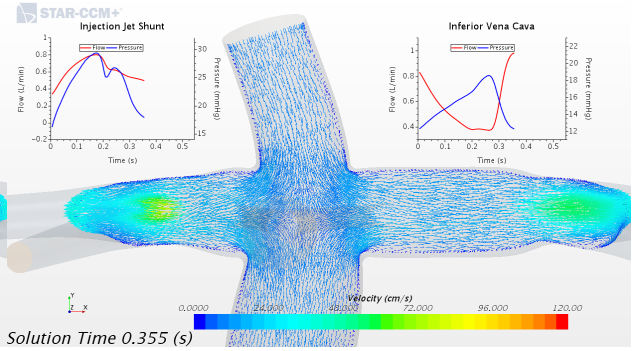

(d) IJS on, -60% PVR

Figure B.7: Velocity vectors during early diastole - anterior view

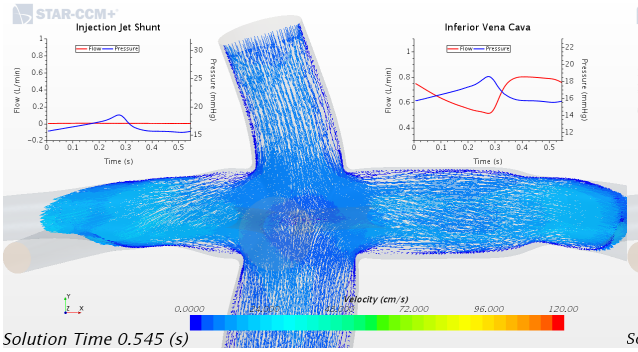

(a) Baseline

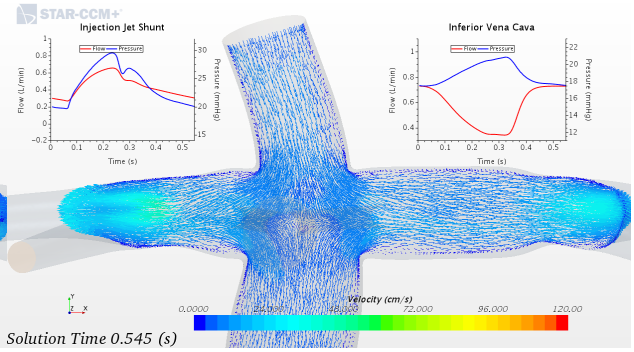

(b) IJS on, Baseline PVR

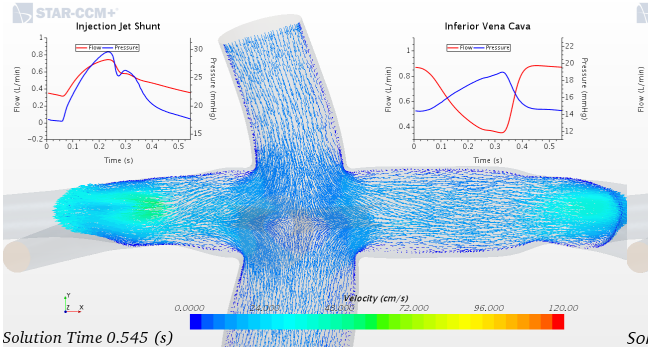

(c) IJS on, -40% PVR

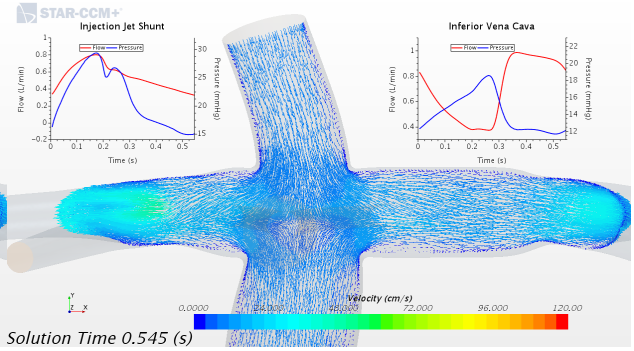

(d) IJS on, -60% PVR

Figure B.8: Velocity vectors during late diastole - anterior view

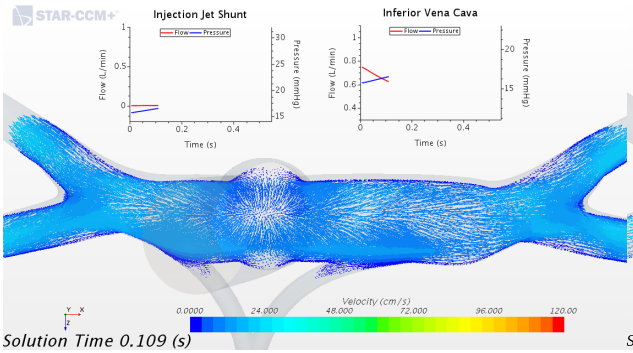

(a) Baseline

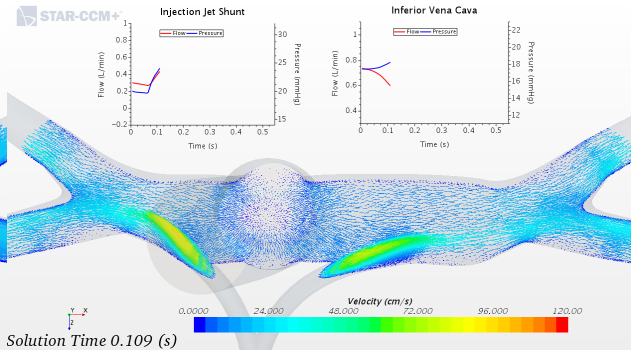

(b) IJS on, Baseline PVR

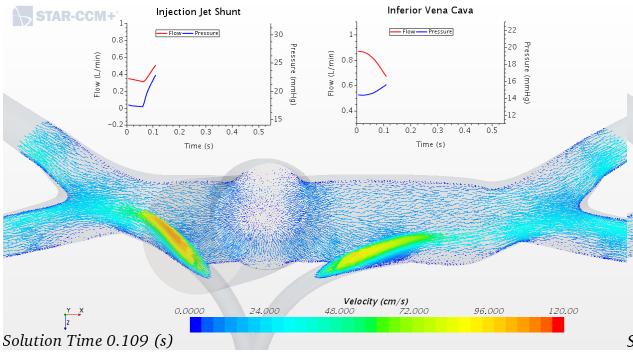

(c) IJS on, -40% PVR

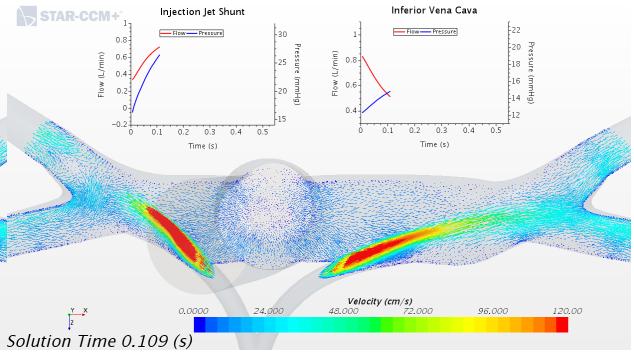

(d) IJS on, -60% PVR

Figure B.9: Velocity vectors during early systole - superior view

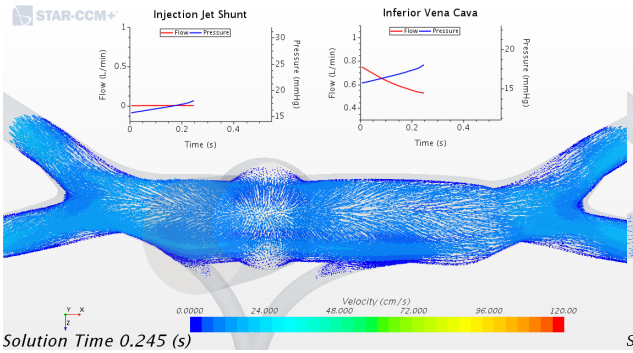

(a) Baseline

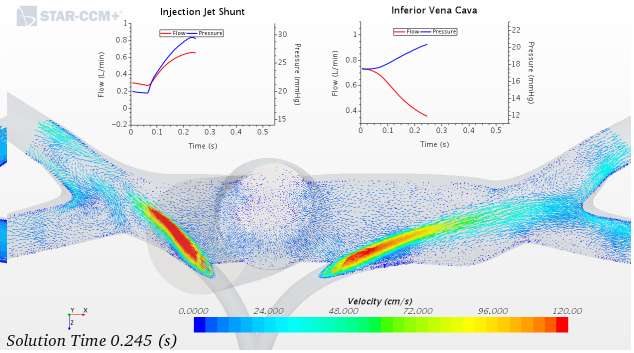

(b) IJS on, Baseline PVR

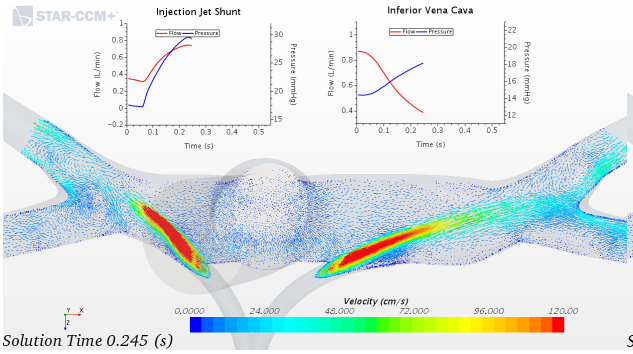

(c) IJS on, -40% PVR

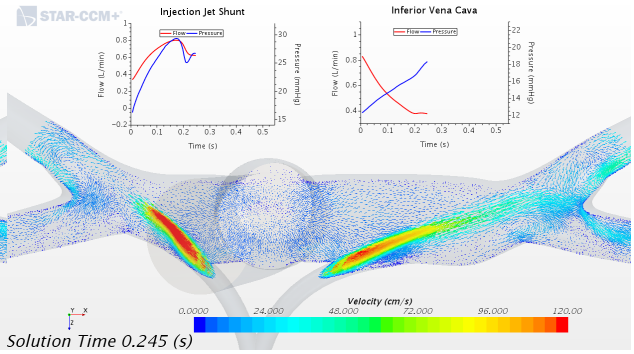

(d) IJS on, -60% PVR

Figure B.10: Velocity vectors during late systole - superior view

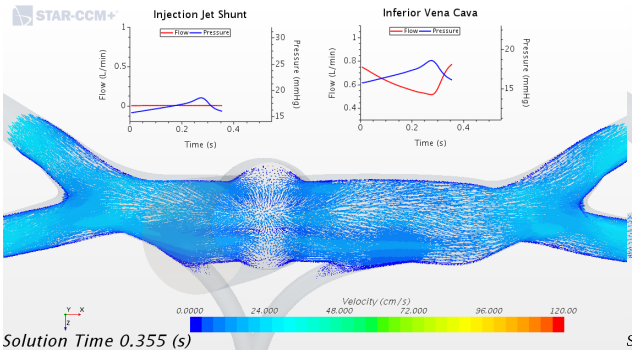

(a) Baseline

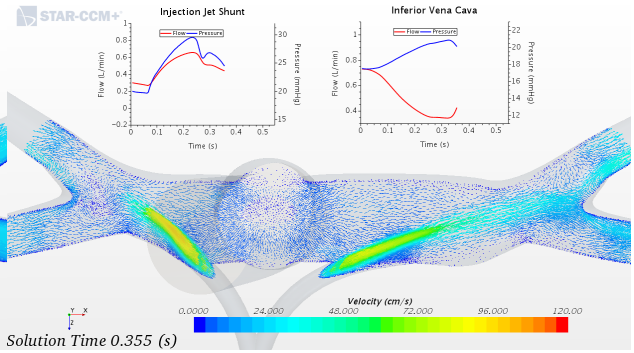

(b) IJS on, Baseline PVR

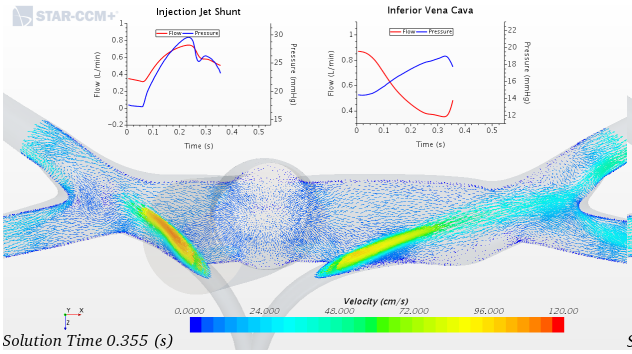

(c) IJS on, -40% PVR

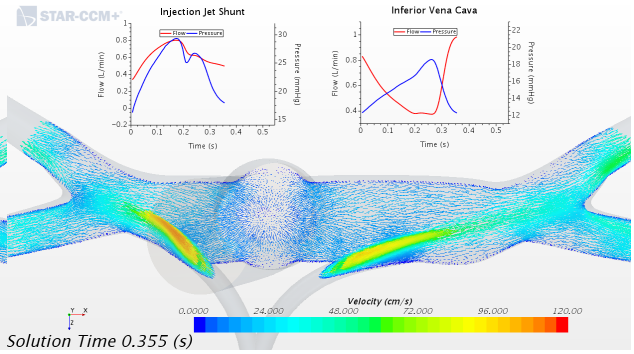

(d) IJS on, -60% PVR

Figure B.11: Velocity vectors during early diastole - superior view

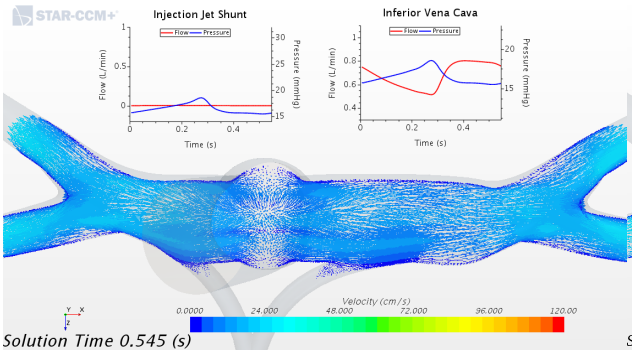

(a) Baseline

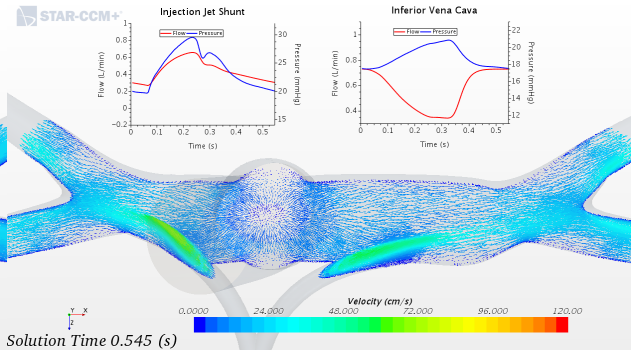

(b) IJS on, Baseline PVR

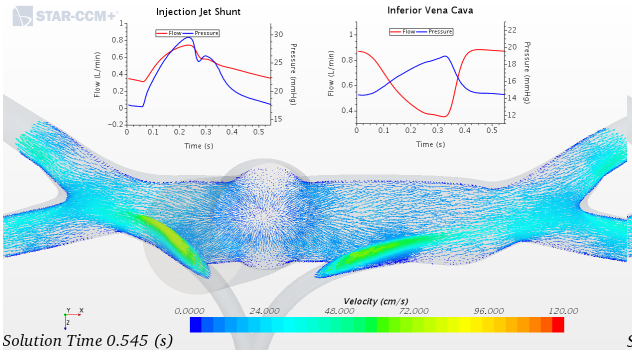

(c) IJS on, -40% PVR

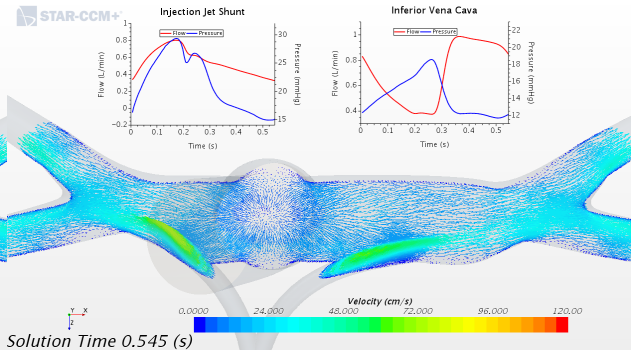

(d) IJS on, -60% PVR

Figure B.12: Velocity vectors during late diastole - superior view

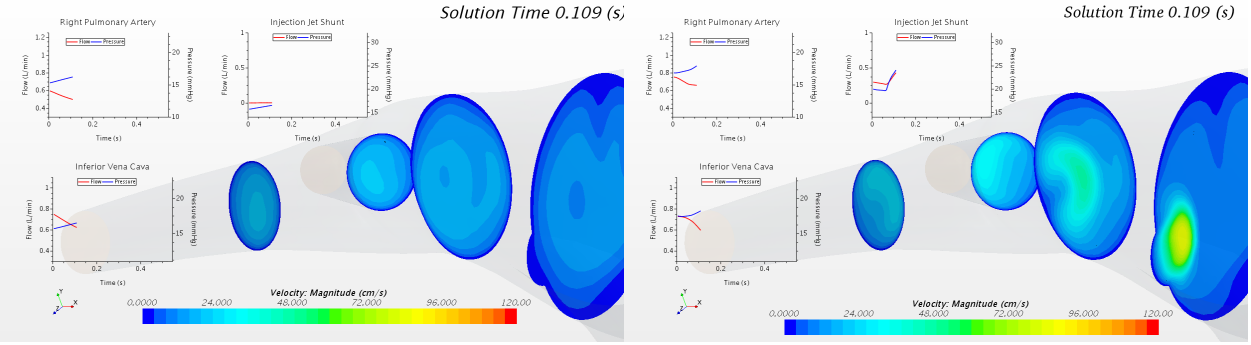

(a) Baseline

(b) IJS on, Baseline PVR

(c) IJS on, -40% PVR

(d) IJS on, -60% PVR

Figure B.13: Velocity magnitudes during early systole - looking down the RPA

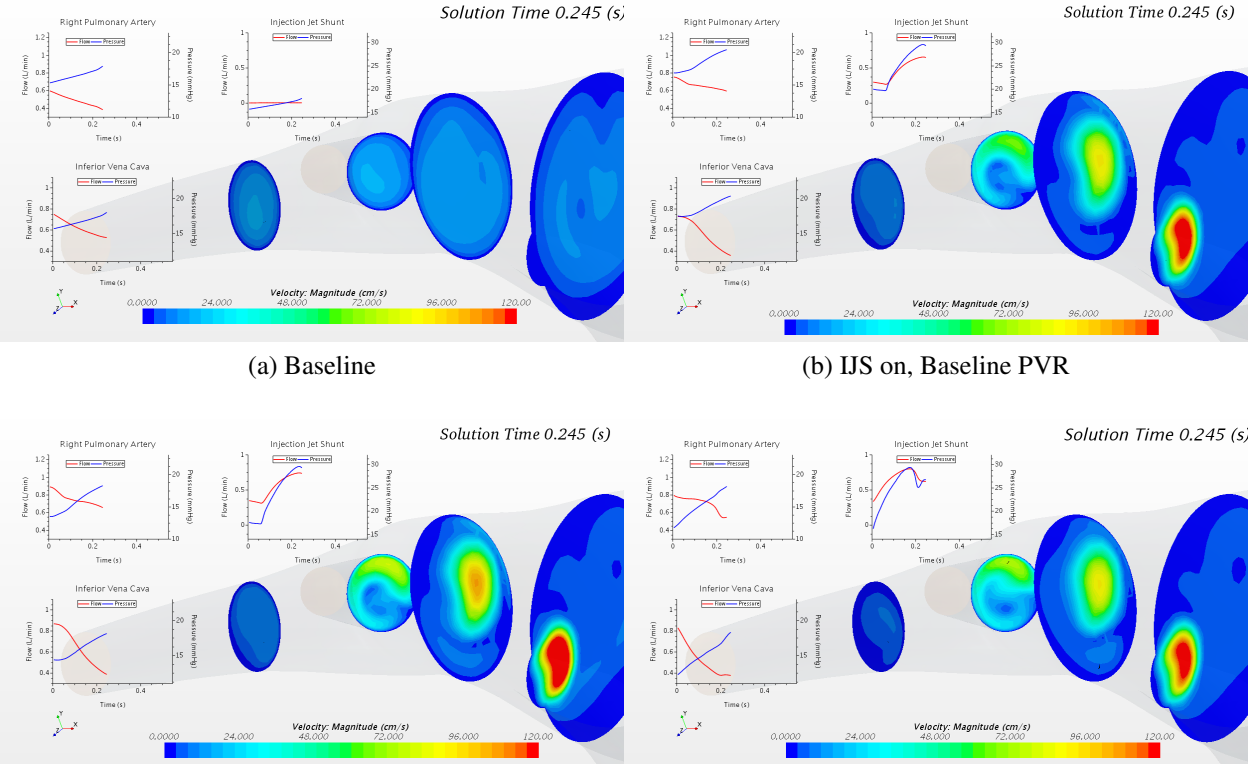

(a) Baseline

(b) IJS on, Baseline PVR

(c) IJS on, -40% PVR

(d) IJS on, -60% PVR

Figure B.14: Velocity magnitudes during late systole - looking down the RPA

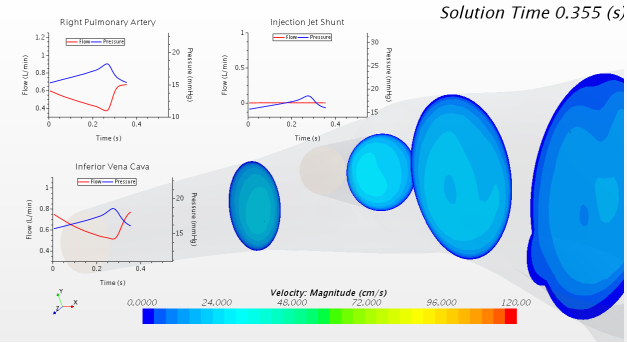

(a) Baseline

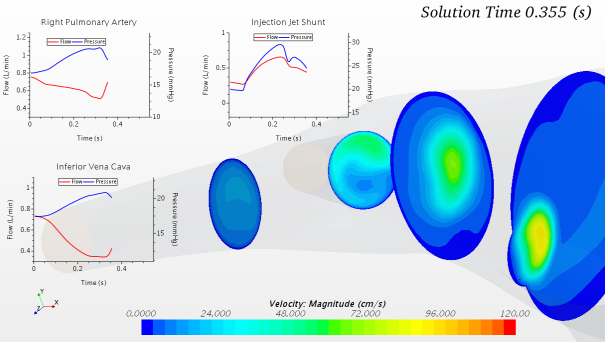

(b) IJS on, Baseline PVR

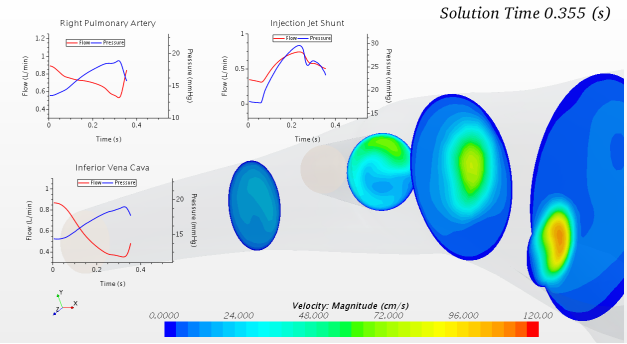

(c) IJS on, -40% PVR

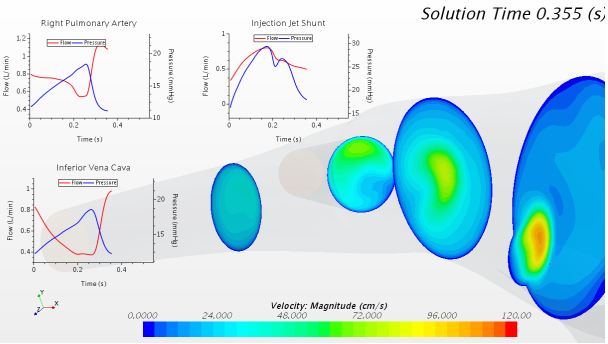

(d) IJS on, -60% PVR

Figure B.15: Velocity magnitudes during early diastole - looking down the RPA

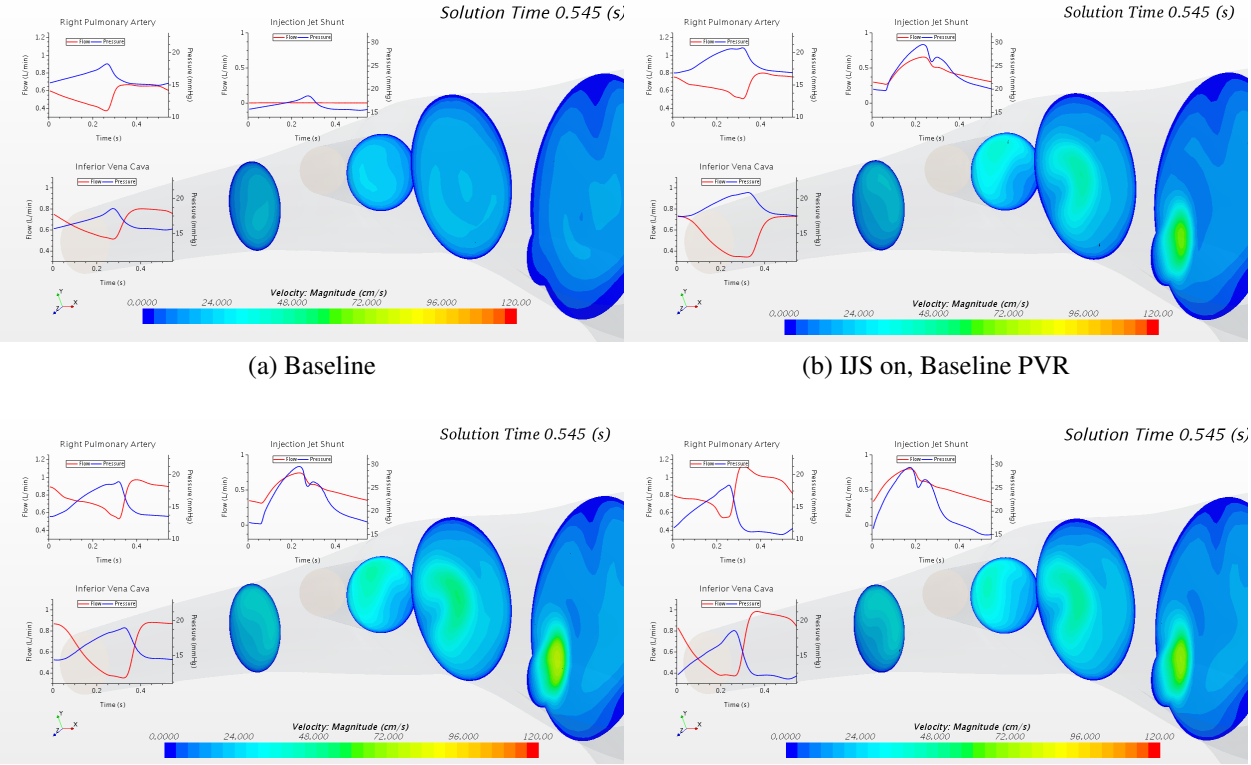

(a) Baseline

(b) IJS on, Baseline PVR

(c) IJS on, -40% PVR

(d) IJS on, -60% PVR

Figure B.16: Velocity magnitudes during late diastole - looking down the RPA

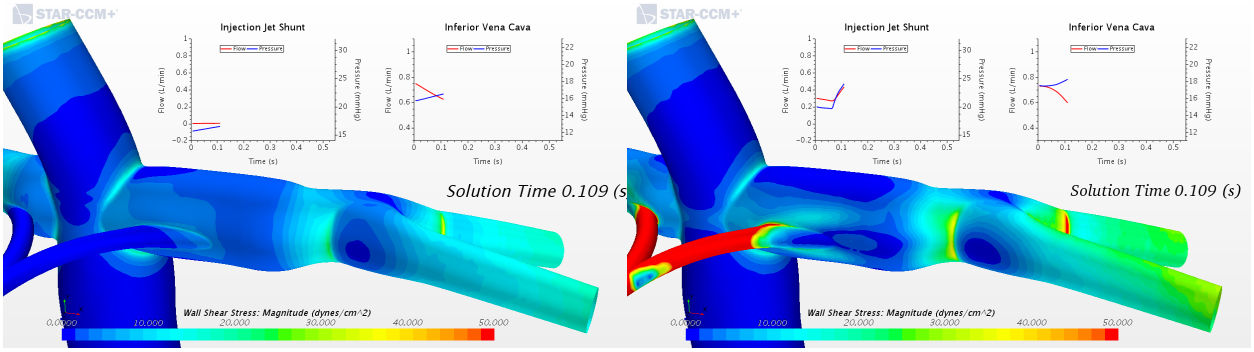

(a) Baseline

(b) IJS on, Baseline PVR

(c) IJS on, -40% PVR

(d) IJS on, -60% PVR

Figure B.17: WSS during early systole

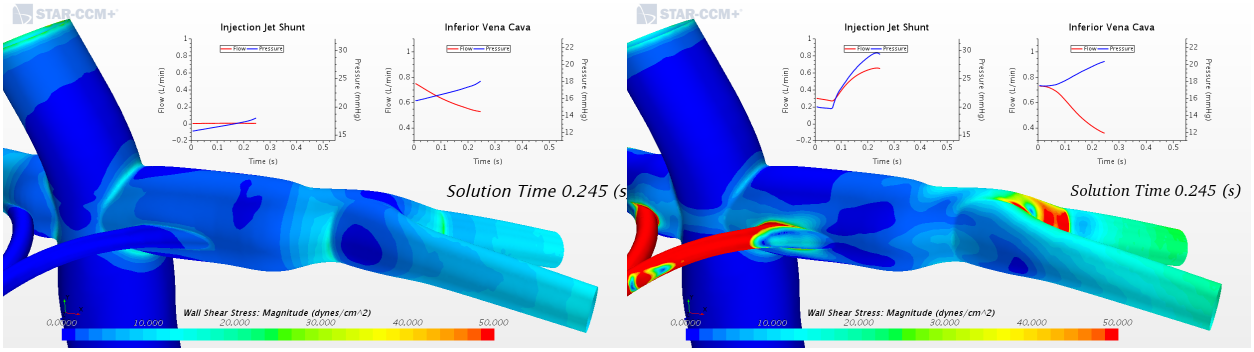

(a) Baseline

(b) IJS on, Baseline PVR

(c) IJS on, -40% PVR

(d) IJS on, -60% PVR

Figure B.18: WSS during late systole

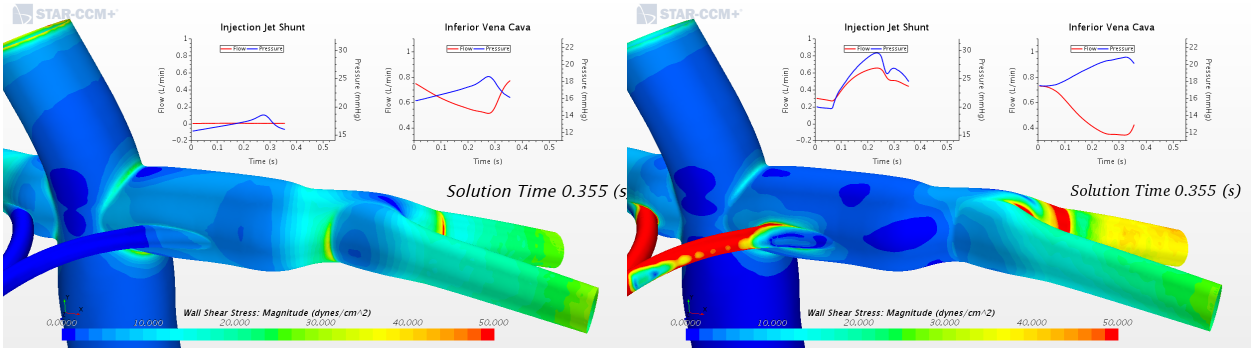

(a) Baseline

(b) IJS on, Baseline PVR

(c) IJS on, -40% PVR

(d) IJS on, -60% PVR

Figure B.19: WSS during early diastole

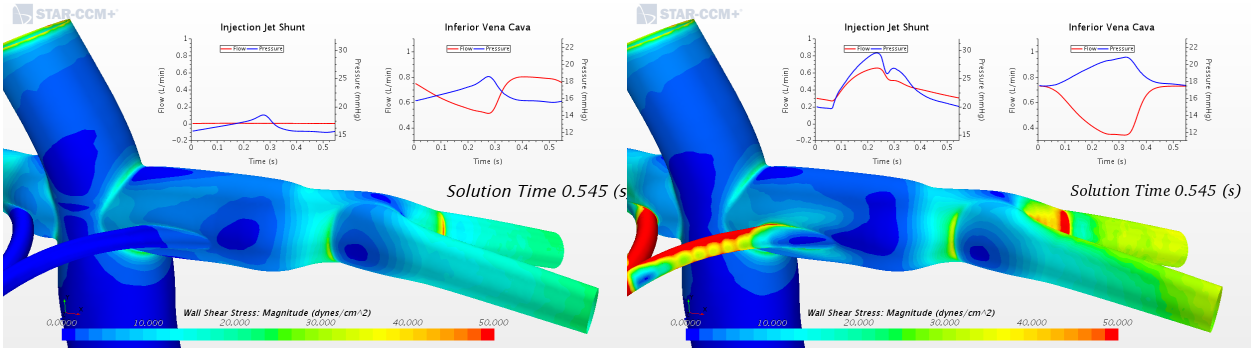

(a) Baseline

(b) IJS on, Baseline PVR

(c) IJS on, -40% PVR

(d) IJS on, -60% PVR

Figure B.20: WSS during late diastole

LIST OF REFERENCES

[1] W C Aird. Spatial and temporal dynamics of the endothelium. *Journal of Thrombosis and Haemostatis*, 3:1392–1406, 2005.

[2] Vladimir Alexi-Meskishvili, Stanislav Ovroutski, Peter Ewert, Ingo Dähnert, Felix Berger, Peter E. Lange, and Roland Hetzer. Optimal conduit size for extracardiac Fontan operation. *European Journal of Cardio-thoracic Surgery*, 18(6):690–695, 2000.

[3] Yuri Bazilevs, M. C. Hsu, D. J. Benson, S. Sankaran, and A. L. Marsden. Computational fluid-structure interaction: Methods and application to a total cavopulmonary connection. *Computational Mechanics*, 2009.

[4] E. L. Bove, M. R. De Leval, F. Migliavacca, R. Balossino, and G. Dubini. Toward optimal hemodynamics: Computer modeling of the Fontan circuit. *Pediatric Cardiology*, 28(6):477–481, 2007.

[5] Andres Ceballos, I. Ricardo Argueta-Morales, Eduardo Divo, Ruben Osorio, Christopher A. Caldarone, Alain J. Kassab, and William M. Decampli. Computational analysis of hybrid Norwood circulation with distal aortic arch obstruction and reverse blalock-taussig shunt. *Annals of Thoracic Surgery*, 94(5):1540–1550, 2012.

[6] Paweena Chungsomprasong, Jarupim Soongswang, Apichart Nana, Kritvikrom Durongpisitkul, Daungmanee Loahaprasitiporn, Chodchanok Vijansorn, and Somchai Sriyodchartti. Medium and long-term outcomes of Fontan operation. *Journal of the Medical Association of Thailand = Chotmaihet thangphaet*, 94(3):323–30, 2011.

[7] M. R. De Leval, G. Dubini, F. Migliavacca, H. Jalali, G. Camporini, A. Redington, and R. Pietrabissa. Use of computational fluid dynamics in the design of surgical procedures:

Application to the study of competitive flows in cavopulmonary connections. *Journal of Thoracic and Cardiovascular Surgery*, 111(3):502–513, 1996.

[8] William M. DeCampli, Virgil Secasanu, I. Ricardo Argueta-Morales, Kelly Cox, Constantine Ionan, and Alain J. Kassab. External counterpulsation of a systemic-to-pulmonary artery shunt increases coronary blood flow in neonatal piglets. *World Journal for Pediatric and Congenital Hearth Surgery*, 6(1):75–82, 2015.

[9] Yann T. Delorme, Mark D. Rodefeld, and Steven H. Frankel. Multiblock high order Large Eddy Simulation of powered Fontan hemodynamics: Towards computational surgery. *Computers and Fluids*, 143:16–31, 2017.

[10] Mahdi Esmaily Moghadam, Yuri Bazilevs, Tain Yen Hsia, Irene E. Vignon-Clementel, and Alison L. Marsden. A comparison of outlet boundary treatments for prevention of backflow divergence with relevance to blood flow simulations. *Computational Mechanics*, 48(3):277–291, 2011.

[11] Mahdi Esmaily Moghadam, Irene E. Vignon-Clementel, Richard Figliola, and Alison L. Marsden. A modular numerical method for implicit 0D/3D coupling in cardiovascular finite element simulations. *Journal of Computational Physics*, 2013.

[12] F Fontan and E Baudet. Surgical repair of tricuspid atresia. *Thorax*, 26, 1971.

[13] Marc Gewillig and Stephen C Brown. The Fontan circulation after 45years: update in physiology. *Heart*, 2016.

[14] Marc Gewillig and David J. Goldberg. Failure of the fontan circulation, 2014.

[15] Bryan H. Goldstein, Chad E. Connor, Lindsay Gooding, and Albert P. Rocchini. Relation of Systemic Venous Return, Pulmonary Vascular Resistance, and Diastolic Dysfunction to

Exercise Capacity in Patients With Single Ventricle Receiving Fontan Palliation. *American Journal of Cardiology*, 105(8):1169–1175, 2010.

[16] Roland Henaine, Mathieu Vergnat, Emile A. Bacha, Bruno Baudet, Virginie Lambert, Emre Belli, and Alain Serraf. Effects of lack of pulsatility on pulmonary endothelial function in the Fontan circulation. *Journal of Thoracic and Cardiovascular Surgery*, 146(3):522–529, 2013.

[17] Julien I.E. Hoffman and Samuel Kaplan. The incidence of congenital heart disease. *Journal of the American College of Cardiology*, 39(12):1890–1900, 2002.

[18] Tain Yen Hsia, Francesco Migliavacca, Simone Pittaccio, Alessandro Radaelli, Gabriele Dubini, Giancarlo Pennati, and Marc De Leval. Computational fluid dynamic study of flow optimization in realistic models of the total cavopulmonary connections. *Journal of Surgical Research*, 116(2):305–313, 2004.

[19] Li Huang, Kim M. Dalziel, Chris Schilling, David S. Celermajer, John J. McNeil, David Winlaw, Tom Gentles, Dorothy J. Radford, Michael Cheung, Andrew Bullock, Gavin R. Wheaton, Robert N. Justo, Lisa A. Selbie, Victoria Forsdick, Karin Du Plessis, and Yves D'Udekem. Hospital costs and cost implications of co-morbid conditions for patients with single ventricle in the period through to Fontan completion. *International Journal of Cardiology*, 240:178–182, 2017.

[20] Keiichi Itatani, Kagami Miyaji, Takahiro Tomoyasu, Yayoi Nakahata, Kuniyoshi Ohara, Shinichi Takamoto, and Masahiro Ishii. Optimal Conduit Size of the Extracardiac Fontan Operation Based on Energy Loss and Flow Stagnation. *Annals of Thoracic Surgery*, 88(2):565–573, 2009.

[21] Yueqian Jia, I. Ricardo Argueta-Morales, Miao Liu, Yuanli Bai, Eduardo Divo, Alain J. Kassab, and William M. Decampli. Experimental study of anisotropic stress/strain relation-

ships of the piglet great vessels and relevance to pediatric congenital heart disease. *Annals of Thoracic Surgery*, 99(4):1399–1407, 2015.

[22] Yueqian Jia, Yangyang Qiao, I Ricardo Argueta-Morales, Aung Maung, Jack Norfleet, Yuanli Bai, Eduardo Divo, Alain J Kassab, and William M Decampli. Experimental Study of Anisotropic Stress/Strain Relationships of Aortic and Pulmonary Artery Homografts and Synthetic Vascular Grafts. *Journal of Biomechanical Engineering*, 2017.

[23] Yasuhiro Kotani, Devin Chetan, Jiaquan Zhu, Arezou Saedi, Lisa Zhao, Luc Mertens, Andrew N. Redington, John Coles, Christopher A. Caldarone, Glen S. Van Arsdell, and Osami Honjo. Fontan Failure and Death in Contemporary Fontan Circulation: Analysis From the Last Two Decades. *Annals of Thoracic Surgery*, 105(4):1240–1247, 2018.

[24] Wei-chih Patrick Lin. *Cavopulmonary Assist Device to Bridge Failing Fontan Circulations*. PhD thesis, University of Toronto, 2018.

[25] C. C. Long, M. C. Hsu, Y. Bazilevs, J. A. Feinstein, and A. L. Marsden. Fluid-structure interaction simulations of the Fontan procedure using variable wall properties. *International Journal for Numerical Methods in Biomedical Engineering*, 2012.

[26] Alison L. Marsden, Adam J. Bernstein, V. Mohan Reddy, Shawn C. Shadden, Ryan L. Spilker, Frandics P. Chan, Charles A. Taylor, and Jeffrey A. Feinstein. Evaluation of a novel Y-shaped extracardiac Fontan baffle using computational fluid dynamics. *Journal of Thoracic and Cardiovascular Surgery*, 137(2):394–403.e2, 2009.

[27] Alison L. Marsden, Irene E. Vignon-Clementel, Frandics P. Chan, Jeffrey A. Feinstein, and Charles A. Taylor. Effects of exercise and respiration on hemodynamic efficiency in CFD simulations of the total cavopulmonary connection. *Annals of Biomedical Engineering*, 35(2):250–263, 2007.

[28] Francesco Migliavacca, Philip J. Kilner, Giancarlo Pennati, Gabriele Dubini, Riccardo Pietrabissa, Roberto Fumero, and Marc Roger De Levai. Computational fluid dynamic and magnetic resonance analyses of flow distribution between the lungs after total cavopulmonary connection. *IEEE Transactions on Biomedical Engineering*, 46(4):393–399, 1999.

[29] Max B. Mitchell, David N. Campbell, Dunbar Ivy, Mark M. Boucek, Henry M. Sondheimer, Biagio Pietra, Bibhuti B. Das, and Joseph R. Coll. Evidence of pulmonary vascular disease after heart transplantation for Fontan circulation failure. *Journal of Thoracic and Cardiovascular Surgery*, 128(5):693–702, 2004.

[30] Thuy Tien Nguyen, I. Ricardo Argueta-Morales, Stephen Guimond, William Clark, Andres Ceballos, Ruben Osorio, Eduardo A. Divo, William M. De Campli, and Alain J. Kassab. Computational analysis of pediatric ventricular assist device implantation to decrease cerebral particulate embolization. *Computer Methods in Biomechanics and Biomedical Engineering*, 19(7):789–799, 2016.

[31] Marcus Ni. *COMPUTATIONAL FLUID DYNAMICS PROOF OF CONCEPT AND ANALYSIS OF A SELF-POWERED FONTAN CIRCULATION*. PhD thesis, 2017.

[32] Marcus W. Ni, Ray O. Prather, Giovanna Rodriguez, Rachel Quinn, Eduardo Divo, Mark Fogel, Alain J. Kassab, and William M. DeCampli. Computational Investigation of a Self-Powered Fontan Circulation. *Cardiovascular Engineering and Technology*, 9(2):202–216, 2018.

[33] Andres F. Osorio, Ruben Osorio, Andres Ceballos, Reginald Tran, William Clark, Eduardo A. Divo, I. Ricardo Argueta-Morales, Alain J. Kassab, and William M. DeCampli. Computational fluid dynamics analysis of surgical adjustment of left ventricular assist device implantation to minimise stroke risk. *Computer Methods in Biomechanics and Biomedical Engineering*, 16(6):622–638, 2013.

[34] Kerem Pekkan, David Frakes, Diane De Zelicourt, Carol W. Lucas, W. James Parks, and Ajit P. Yoganathan. Coupling pediatric ventricle assist devices to the Fontan circulation: Simulations with a lumped-parameter model. *ASAIO Journal*, 51(5):618–628, 2005.

[35] Ray Prather, Alain J. Kassab, Marcus Ni, Eduardo A. Divo, Ricardo Argueta-Morales, and William M. DeCampli. Multi-scale pulsatile CFD modeling of thrombus transport in a patient-specific LVAD implantation. *International Journal of Numerical Methods for Heat & Fluid Flow*, 2017.

[36] Alfio Quarteroni, Stefania Ragni, and Alessandro Veneziani. Coupling between lumped and distributed models for blood flow problems. *Computing and Visualization in Science*, 2001.

[37] Mark D. Reller, Matthew J. Strickland, Tiffany Riehle-Colarusso, William T. Mahle, and Adolfo Correa. Prevalence of Congenital Heart Defects in Metropolitan Atlanta, 1998-2005. *Journal of Pediatrics*, 153(6):807–813, 2008.

[38] I. Ricardo Argueta-Morales, Reginald Tran, Andres Ceballos, William Clark, Ruben Osorio, Eduardo A. Divo, Alain J. Kassab, and William M. DeCampli. Mathematical Modeling of Patient-Specific Ventricular Assist Device Implantation to Reduce Particulate Embolization Rate to Cerebral Vessels. *Journal of Biomechanical Engineering*, 136(7):071008, 2014.

[39] Chris Schilling, Kim Dalziel, Russell Nunn, Karin Du, William Y Shi, David Celermajer, David Winlaw, Robert G Weintraub, Leanne E Grigg, Dorothy J Radford, Andrew Bullock, Thomas L Gentles, Gavin R Wheaton, Tim Hornung, and Robert N Justo. The Fontan epidemic: Population projections from the Australia and New Zealand Fontan Registry. *International Journal of Cardiology*, 219:14–19, 2017.

[40] Boris Schmitt, Paul Steendijk, Stanislav Ovroutski, Karsten Lunze, Pedram Rahmanzadeh, Nizar Maarouf, Peter Ewert, Felix Berger, and Titus Kuehne. Pulmonary vascular resistance,

collateral flow, and ventricular function in patients with a fontan circulation at rest and during dobutamine stress. *Circulation: Cardiovascular Imaging*, 3(5):623–631, 2010.

[41] Shuji Shimizu, Toru Kawada, Dai Une, Masafumi Fukumitsu, Michael James Turner, Atsunori Kamiya, Toshiaki Shishido, and Masaru Sugimachi. Partial cavopulmonary assist from the inferior vena cava to the pulmonary artery improves hemodynamics in failing Fontan circulation: a theoretical analysis. *Journal of Physiological Sciences*, 66(3):249–255, 2016.

[42] Martin Spiegel, Thomas Redel, Y Zhang, Tobias Struffert, Joachim Hornegger, Robert G Grossman, Arnd Doerfler, and Christof Karmonik. Tetrahedral and polyhedral mesh evaluation for cerebral hemodynamic simulation–a comparison. *Conference proceedings : ... Annual International Conference of the IEEE Engineering in Medicine and Biology Society. IEEE Engineering in Medicine and Biology Society. Conference*, 2009:2787–90, 2009.

[43] N Stergiopulos, J J Meister, and N Westerhof. Determinants of stroke volume and systolic and diastolic aortic pressure. *The American journal of physiology*, 270:H2050–H2059, 1996.

[44] Jeong Jin Yu, Tae Jin Yun, Sung Cheol Yun, Yu Mi Im, Seung Chul Lee, Hong Ju Shin, Hong Ki Ko, Jeong Jun Park, Dong Man Seo, Young Hwue Kim, Jae Kon Ko, and In Sook Park. Low pulmonary vascular compliance predisposes post-Fontan patients to protein-losing enteropathy. *International Journal of Cardiology*, 165(3):454–457, 2013.